Journal of Nanobiotechnology

RESEARCH Open Access

Erythrocyte membrane camouflaged celastrol and bilirubin self-assembly for rheumatoid arthritis immunotherapy based on STING inhibition and RONS clearance

Yanguo Su[1], Rui Chen[1], Bingjie Wang[1], Teng Wang[1], Jiaojiao Tao[1], Qijie Diao[1], Tianze Jiang[1] and Xia Zhao[1,2*]

Abstract
Activation of cGAS-STING signaling pathway and accumulation of reactive oxygen and nitrogen species (RONS) are important issues facing the treatment of rheumatoid arthritis (RA). Here, we report a biomimetic nano-Chinese medicine (HA-RM-Cel-BR) for RA immunotherapy based on STING inhibition of celastrol (Cel) and RONS clearance of bilirubin (BR). HA-RM-Cel-BR is constructed by the carrier-free self-assembly of active ingredients Cel and BR from traditional Chinese medicine, and then camouflaged by hyaluronic acid (HA)-modified red blood cell membranes (RM). HA-RM-Cel-BR prolongs circulation time through RM camouflage, targets inflamed joints by HA modification, and remodels the joint immune microenvironment by STING inhibition and RONS clearance. More importantly, HA-RM-Cel-BR shows excellent therapeutic effects on RA rat model, and significantly reduces hepatotoxicity associated with Cel. Our work provides a new strategy for RA immunotherapy with traditional Chinese medicine ingredients.

Keywords Red blood cell membranes, Macrophage polarization, Immune microenvironment, Hepatotoxicity, Hyaluronic acid

Introduction

Rheumatoid arthritis (RA) is a chronic, systemic autoimmune disease characterized by synovitis, cartilage loss, and bone erosion, which can even lead to disability [1]. Current first-line drugs for RA treatment include corticosteroids (such as dexamethasone) [2] and disease-modifying anti-rheumatic drugs (such as methotrexate) [3]. However, these drugs fail to maintain the immune balance of RA lesion sites, and are not effective in preventing the ongoing joint damage [4]. Additionally, high doses and frequent administration of these drugs often lead to adverse side effects [5]. Compared with hormones and chemical drugs, traditional Chinese medicine (TCM) shows unique advantages in RA treatment [6, 7]. In particular, the TCM theory of "Fu zheng" (strengthening the body resistance) and "Qu xie" (eliminating pathogenic factors) is highly consistent with the objective of immune modulation and inflammation inhibition in modern RA treatment [8]. Therefore, it is of great significance to develop new TCM formulations for RA treatment.

Recent studies have shown that activation of cGAS-STING signaling pathway [9] and accumulation of reactive oxygen and nitrogen species (RONS) promote the polarization of M1 macrophages [10], leading to articular cartilage destruction and bone damage. Moreover,

*Correspondence:
Xia Zhao
zhaoxia@ouc.edu.cn
[1]Key Laboratory of Marine Drugs, School of Medicine and Pharmacy, Ministry of Education, Ocean University of China, Qingdao 266003, China
[2]Laboratory for Marine Drugs and Bioproducts, Qingdao Marine Science and Technology Center, Qingdao 266237, China

RONS cause damage to cellular components such as proteins, lipids, and DNA, triggering the production of new autoantigens, which are key factors in the development of RA [11, 12]. It has been reported that STING pathway inhibitors can effectively modulate immune response and reduce excessive inflammation [13, 14], showing great potential in anti-inflammatory, especially in the treatment of RA. While natural antioxidants derived from TCM, such as curcumin [15] and quercetin [16], have been shown to have significant RNOS clearance and anti-inflammatory effects with few side effects. Therefore, natural active ingredients derived from TCM that can effectively clear RONS and inhibit STING pathway may be a promising therapeutic strategy for RA treatment.

Tripterygium wilfordii is widely used for the treatment of autoimmune diseases in China due to its immune regulation ("Fu zheng" in TCM theory) [17]. Celastrol (Cel), as a key component of *Tripterygium wilfordii*, has been shown to exert anti-inflammatory effects by inhibiting STING pathway [18]. However, the poor water solubility, low bioavailability, and drug-induced liver injury of Cel limit its clinical application [19]. Despite nanotechnology can improve Cel delivery, there are still problems such as limited drug loading capacity and unavoidable side effects of additional excipients [20, 21].

According to TCM theory, RA is associated with the concept of "heat toxins" in the body. *Calculus bovis* is known to clear "heat toxins" [22], enhance liver detoxification, and inhibit inflammation ("Qu xie" in TCM theory) [23], which is beneficial for alleviating joint inflammation and pain. Studies have found that bilirubin (BR), as the active ingredient of *calculus bovis*, can eliminate RONS, inhibit inflammation [24] and mitigate liver damage caused by oxidative stress [25]. However, due to the poor water solubility and low bioavailability of BR, its clinical application is limited [22].

Recently, carrier-free nanomedicines have attracted wide attention as a novel strategy for disease treatment [8, 26–28]. However, it is a great challenge to develop self-assembled nanomedicines by seeking active ingredients with suitable structure and physicochemical property from TCM. To our knowledge, the self-assembled carrier-free nanomedicines from active components of TCM are rarely reported for RA immunotherapy. Moreover, the nanomedicines are easily cleared by the reticuloendothelial system (RES) once they enter the bloodstream.

Red blood cell membranes (RM) have attracted much attention due to their low immunogenicity and their ability to interact with signal-regulating protein α1 on macrophages, which can inhibit phagocytosis and prolong circulation time [29–31]. Additionally, hyaluronic acid (HA)-modified cell membranes have been reported to specifically target M1 macrophages that overexpress CD44 receptors, thereby enhancing the efficacy of targeted therapy [32].

Here, we develop a biomimetic nano-Chinese medicine system (HA-RM-Cel-BR) for RA treatment, which is composed of carrier-free self-assembled nanomedicines (Cel-BR) of Cel and BR and coated with RM modified with hyaluronic acid (HA) (Scheme 1A). We hypothesize that HA-RM-Cel-BR can prolong blood circulation of Cel-BR by RM coating, and can be targeted to inflamed joints by HA modification. By combining the STING inhibition of Cel and the RONS clearance of BR, it will be beneficial to remodel the joint microenvironment (Scheme 1B). Moreover, the RONS clearance of BR is expected to reduce liver inflammation and toxicity caused by free Cel. We believe that this biomimetic nanomedicine system based on TCM theory and modern drug delivery technology will provide a promising strategy to enhance the efficacy of RA treatment while minimizing toxicity.

Results and discussion

Preparation and characterization of Cel-BR and HA-RM-Cel-BR

Based on the toxicity of Free Cel and the ROS scavenging evaluation of BR (Figures S1-S3), we investigated the self-assembly of nanomedicine Cel-BR using Cel and BR at mass ratios of 1:10, 1:15, and 1:20. Interestingly, all three different ratios produced stable Cel-BR with obvious Tyndall effect (Figure S5). The assembled Cel-BR showed the most effective ROS scavenging capability when the mass ratio of Cel and BR was 1:20 (Figure S4), and the encapsulation efficiency (EE) of Cel reached 97.57 ± 0.85% (Table S1), and the critical aggregation concentration (CAC) of Cel-BR in aqueous solution was 1.39 μg/mL (Fig. 1j). The stability of self-assembly in PBS and 10% FBS solutions at three different ratios was evaluated (Figure S7-S8). The results showed that Cel and BR have better stability at 1:20 than 1:10 and 1:15 in PBS and 10% FBS solutions. In addition, we evaluated the kinetic analysis of Cel and BR through molecular dynamics simulations (Figure S9). The experimental results showed that the nanostructure formed at 1:20 were more stable than those formed at 1:10 and 1:15. Therefore, we chose the ratio of Cel to BR at 1:20 for the subsequent study. Therefore, Cel-BR was prepared according to the mass ratio of 1:20 for the subsequent research.

As shown in Fig. 1a, HA-RM-Cel-BR was synthesized at a mass ratio of Cel-BR to RM of 2:1 and then modified with DSPE-PEG-HA. The particle sizes of Cel-BR, HA-RM-Cel-BR, and HA-RM-Cel-BR were 77.1 ± 1.01, 108 ± 2.25, and 111.7 ± 1.02 nm, respectively (Fig. 1b, S5, S6). Their zeta potentials were – 26.3 ± 1.05, -19.03 ± 1.13 and – 28.56 ± 1.09 mV, respectively (Fig. 1c). The particle size of RM-Cel-BR increased by approximately 31 nm

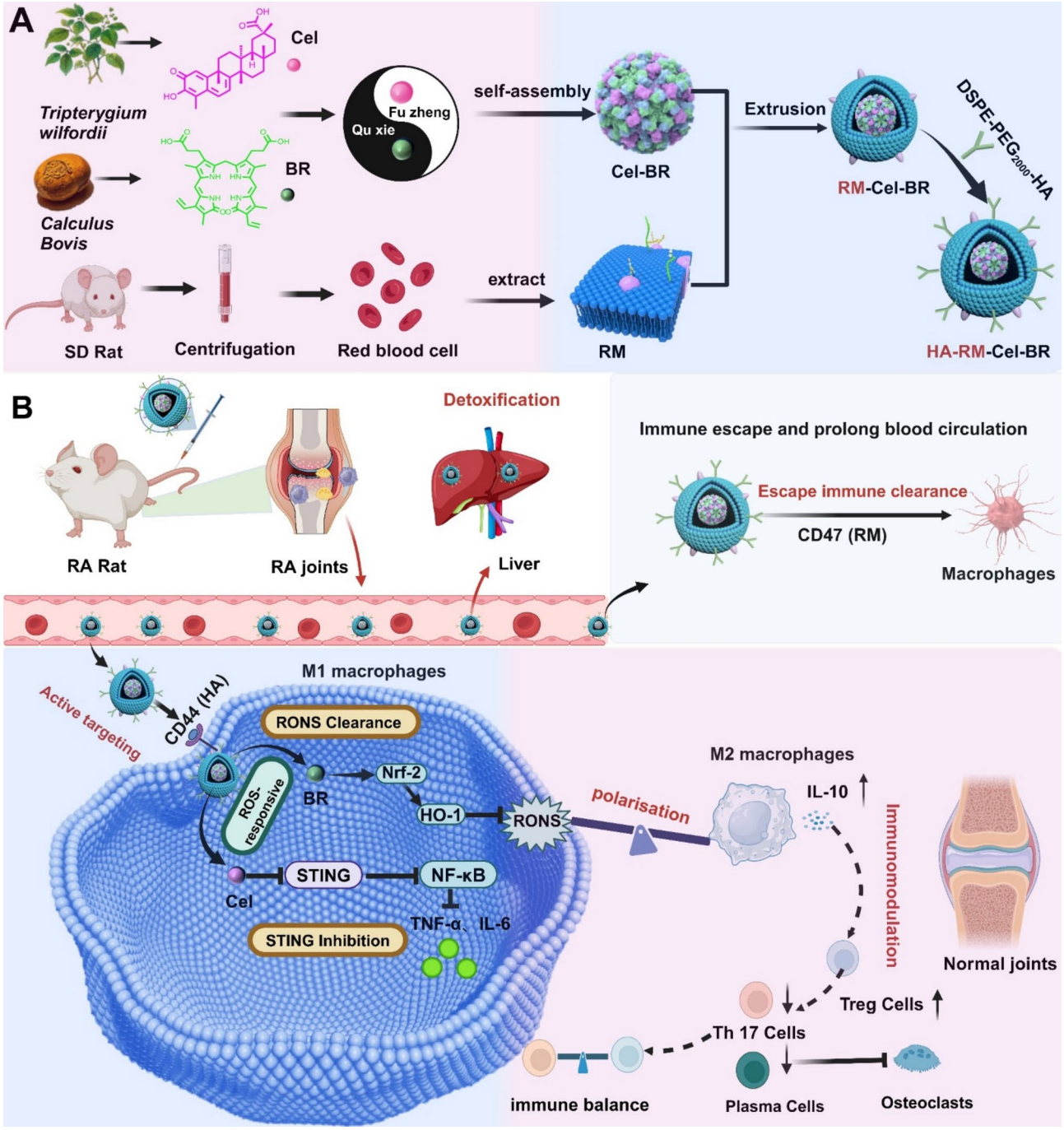

Scheme 1 Schematic diagram of preparation and mechanism of HA-RM-Cel-BR. (**A**) Preparation of HA-RM-Cel-BR. (**B**) HA-RM-Cel-BR escapes immune clearance and prolongs circulation time by RM encapsulation, targets inflamed joints by HA modification, and reduces inflammation by STING inhibition of Cel and RONS clearance of BR. HA-RM-Cel-BR remodels the joint immune microenvironment by promoting macrophage polarization from M1 to M2, recruiting regulatory T cells, and inhibiting helper T cell 17 generation. Created with BioRender.com

compared to that of Cel-BR, which is comparable to the thickness of RM [29–31, 33, 34]. Additionally, the zeta potential of RM-Cel-BR was similar to that of RM, suggesting the successful encapsulation of RM on the surface of Cel-BR. When RM-Cel-BR was modified by DSPE-PEG-HA, the particle size increased slightly and the Zeta potential increased, which may be attributed to the interaction of phospholipid charges in DSPE-PEG-HA. Transmission electron microscopy (TEM) confirmed the successful extraction of the RM (Fig. 1d). TEM showed that Cel-BR was a globular structure (Fig. 1e), while HA-RM-Cel-BR displayed a core-shell structure (Fig. 1f-g),

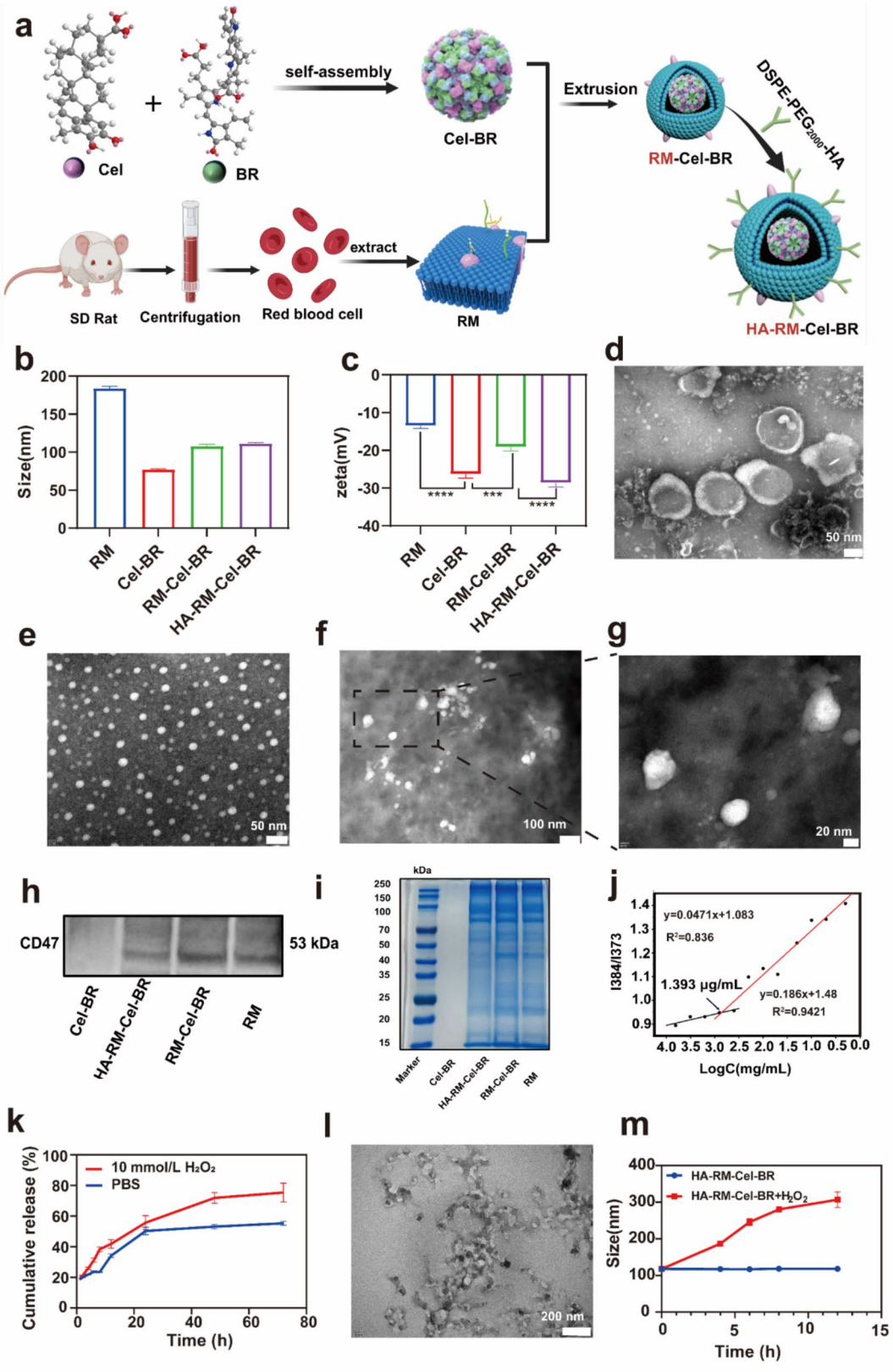

Fig. 1 (See legend on next page.)

(See figure on previous page.)

Fig. 1 Preparation and characterization of HA-RM-Cel-BR. (**a**) Schematic illustration of preparation process of HA-RM-Cel-BR; (**b**) Changes in particle size of different formulations; (**c**) Changes in zeta potential of different formulations; (**d**) TEM image of RM, scale bar = 50 nm; (**e**) TEM image of Cel-BR, scale bar = 50 nm; (**f**) TEM image of HA-RM-Cel-BR, scale bar = 100 nm; (**g**) Partial enlarged view of Figure f, scale bar = 20 nm; (**h**) Western blot analysis of RM protein retention on HA-RM-Cel-BR; (**i**) Coomassie blue assay of RM protein retention on HA-RM-Cel-BR; (**j**) Critical assembly concentration of Cel-BR in aqueous solution. (**k**) Cumulative release of Cel from HA-RM-Cel-BR under PBS and 10 mM H_2O_2 conditions. (**l**) TEM image of HA-RM-Cel-BR after incubation with H_2O_2, scale bar = 200 nm; (**m**) Particle size change of HA-RM-Cel-BR over time in aqueous solution and 10 mM H_2O_2. Data are presented as mean ± SD ($n = 3$). *$P < 0.05$, **$P < 0.01$, and ***$P < 0.001$

indicating the successful encapsulation of Cel-BR by RM. The results of Caulmers Brilliant Blue staining and Western blot analysis showed that the normal function of RM did not change significantly during the preparation process (Figs. 1h-i), and the immune escape-associated CD47 protein remained highly expressed, which is beneficial for escaping immune system clearance.

In addition, the stability of HA-RM-Cel-BR was evaluated (Figure S10). The experimental results showed that the particle size of HA-RM-Cel-BR in PBS did not change significantly within 7 days. The particle size of HA-RM-Cel-BR in 10% FBS solution was larger than that in PBS solution may due to the formation of protein crown, but it maintained its stability within 7 days. These results indicated that HA-RM-Cel-BR had good stability under physiological conditions.

The cumulative release rate of Cel was 55.28 ± 1.26% under normal phosphate-buffered saline (PBS) conditions after 72 h, while the cumulative release rate of Cel increased to 75.37 ± 6.14% under 10 mmol/L hydrogen peroxide (H_2O_2) solution, indicating that the drug release of HA-RM-Cel-BR is ROS responsive (Fig. 1k). TEM showed that Cel-BR nanoparticles were significantly disrupted after incubation with H_2O_2, further confirming their ROS responsiveness (Fig. 1l). To further demonstrate the ROS responsiveness of HA-RM-Cel-BR, we measured its particle size change over time in aqueous solution and 10 mM H_2O_2. Results showed that the particle size increased with time under H_2O_2 condition, indicating that HA-RM-Cel-BR has ROS response ability (Fig. 1m).

Cel-BR was characterized by ultraviolet (UV-vis) and infrared (FT-IR) spectroscopy. When Cel and BR were physically mixed at a mass ratio of 1:20, the UV-vis spectra showed a maximum absorption peak of 455 nm, while the maximum absorption peak shifted to 440 nm after self-assembly into nanoparticles (Fig. 2a), indicating the formation of nanostructure of Cel and BR. The UV-vis spectra of RM, Cel-BR, RM-Cel-BR, and HA-RM-Cel-BR (Fig. 2b) showed that the characteristic absorption of Cel-BR remained unchanged after RM encapsulation and DSPE-PEG-HA modification. In addition, FT-IR spectra showed that the leading absorption bands of BR in Cel-BR shifted from 1697.80 cm^{-1} (υ-OH) to 1691.31 cm^{-1}, suggesting the presence of intermolecular hydrogen bonding in Cel-BR complex (Fig. 2c).

Self-Assembly mechanism of Cel-BR

To elucidate the mechanism of Cel and BR assembled into nanoparticles, molecular dynamics (MD) simulation analysis was performed. The Cel and BR molecules progressively aggregated to form stable nanoparticles within 100 ns (Fig. 2d). The root mean square deviation (RMSD) of the MD-simulated system was 4.074 nm (Fig. 2g), indicating that the system was stable in the simulation process. The solvent-accessible surface area (SASA) was used to evaluate the compactness of Cel-BR nanoparticles. The SASA value decreased significantly from 1360.98 nm^2 to 413.16 nm^2 within 40 ns, indicating that Cel and BR had self-assembled into compact nanoparticles (Fig. 2e). The MD analysis showed that π-π stacking interaction was more significant than hydrogen bonding interaction (Fig. 2f, i, j), indicating that the π-π stacking interaction was the main driving force for the formation of Cel-BR nanoparticles. Obvious diffraction peaks were observed at 2θ = 8.6°, 23.92°, 26.4°, 27.2° in the XRD pattern of Cel-BR, respectively (Figure S11). We speculate that the low-angle peaks at 8.6° may correspond to the molecular layering or long-period ordered structure of Cel-BR. Regional peaks of 23°-27 ° may be derived from aromatic ring π-π stacks or short-range ordered structures formed by intermolecular hydrogen bond networks. These results suggested that Cel-BR form stable self-assembled nanostructures may through non-covalent bonding.

In addition, hydrogen nuclear magnetic resonance spectroscopy (^{1}H-NMR) was further employed to investigate the interaction between Cel and BR molecules. Free Cel, free BR, and a physical mixture of Cel and BR (Cel + BR) were dissolved in dimethyl sulfoxide-d6 (DMSO-d_6) with different concentrations of deuterium oxide (D_2O), respectively. The chemical shifts of the hydrogen atoms (labeled a to j) of pentacyclic triterpene in the free Cel molecules gradually shifted to the high field (the right side of the spectrum) with the increase of D_2O concentration (Figure S12a). Similarly, the chemical shifts of the hydrogen atoms (h, i) of pyrrole in the free BR molecules showed a comparable trend to shift to high field (Figure S12b). When Cel and BR were mixed (Cel + BR) in solvents with different D_2O concentrations, the proton peaks of both pentacyclic triterpene ring (proton peak labeled as a') and pyrrole ring (proton peak labeled as b') shifted to high field about 0.02 ppm (Fig. 2h) with the increase of D_2O concentration, indicating that

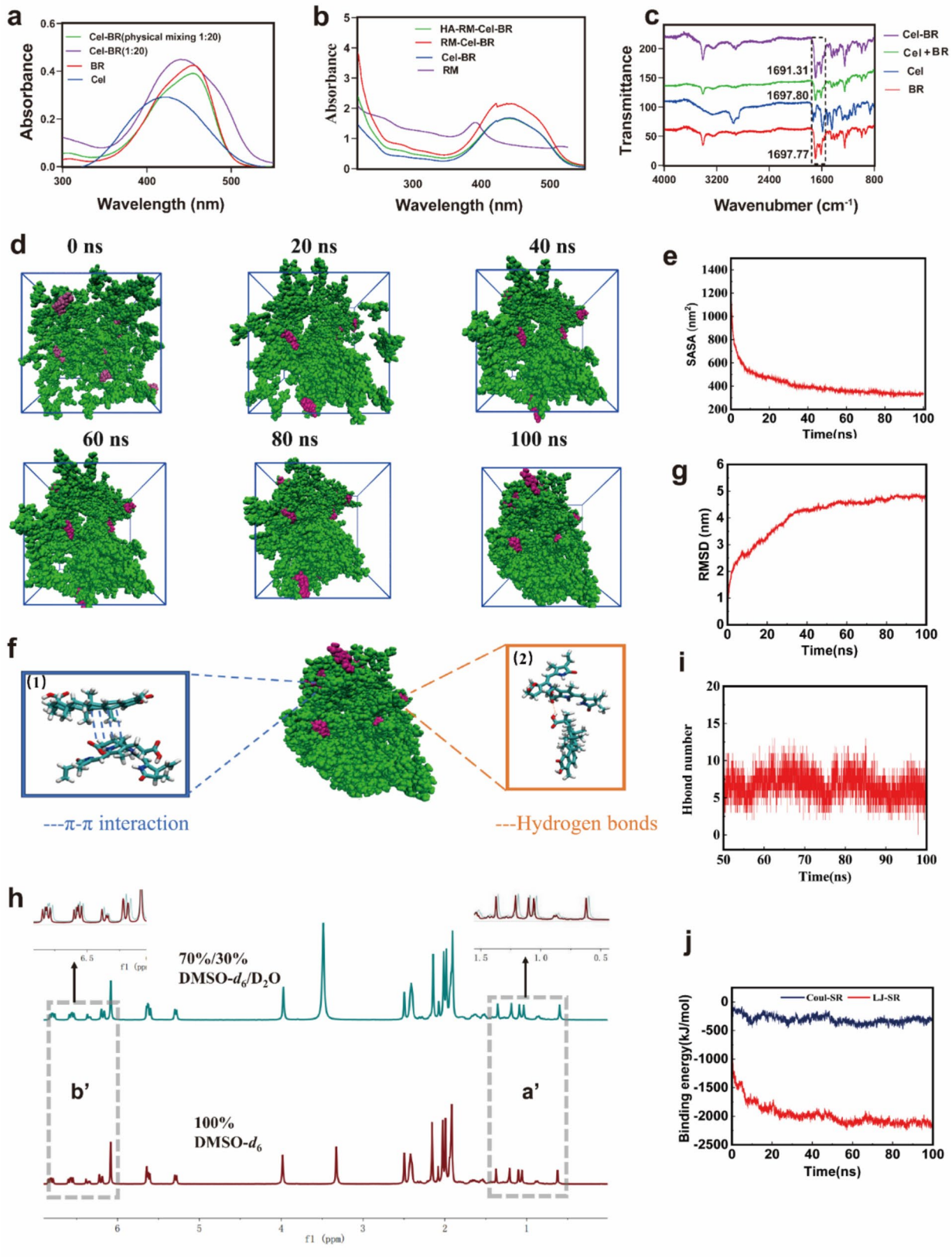

Fig. 2 (See legend on next page.)

(See figure on previous page.)

Fig. 2 Characterization and molecular dynamics simulation of Cel-BR. (**a**) UV-Vis spectra of Cel, BR, the physical mixture of Cel and BR, and Cel-BR. (**b**) UV-Vis spectra of RM, HA-RM-Cel-BR, and Cel-BR. (**c**) Fourier-transform infrared spectra of Cel, BR, the physical mixture of Cel and BR (Cel + BR), and Cel-BR. (**d**) Time-dependent structure evolution of Cel-BR during simulation. (**e**) Solvent-accessible surface area (SASA) of Cel-BR during simulation. (**f**) Interaction patterns between molecules in Cel-BR. (**g**) Root mean square deviation (RMSD) of all atoms in Cel-BR during simulation. (**h**) ^{1}H-NMR spectra of Cel + BR in DMSO-d6 with different D_2O concentrations. (**i**) Time-dependent variation of intermolecular hydrogen bonds in Cel-BR during simulation. (**j**) Changes in intermolecular binding energy in Cel-BR during simulation

Cel and BR may have specific interaction between pentacyclic triterpene ring and pyrrole ring.

Biocompatibility and targeting evaluation of HA-RM-Cel-BR in vitro

Cel-BR and HA-RM-Cel-BR showed good safety in RAW264.7 cells (Fig. 3a-b) and Fibroblast synovial cells (FLS) (Fig. 3c-d) when the concentration of Cel was 200 ng/mL. To evaluate the targeting efficacy of HA-RM-Cel-BR toward M1 macrophages, M1 macrophages were induced by lipopolysaccharide (LPS) and cellular uptake was determined by Cou6 fluorescent labeling. HA-RM-Cel-BR@Cou6 showed significantly higher fluorescence intensity than that of Cel-BR@Cou6 (Fig. 3e), and quantitative flow cytometry analysis also showed a statistically significant difference between HA-RM-Cel-BR@Cou6 and Cel-BR@Cou6 (Fig. 3f-g, $P < 0.01$). These results suggest that the affinity of HA to the overexpressed CD44 receptor on the surface of M1 macrophages enhanced the targeting of Cel-BR. The formulations of Cel-BR@Cou6, RM-Cel-BR@Cou6, and HA-RM-Cel-BR@Cou6 were prepared using coumarin 6 (Cou6) as a fluorescent dye to assess their immune escape ability against M0 macrophages. The cells treated with Cel-BR@Cou6 showed strong green fluorescence, while those treated with RM-Cel-BR@Cou6 and HA-RM-Cel-BR@Cou6 showed weaker fluorescence (Fig. 3h-j), indicating that RM encapsulation effectively evaded clearance by RES.

Evaluation of the mechanism of HA-RM-Cel-BR cell internalization and clearance of ROS and NO in vitro

The internalization of HA-RM-Cel-BR by RAW264.7 cells was investigated, and the results showed that its internalization pathway was mainly realized by clathrin-mediated endocytosis (Fig. 4a, S13). The reactive oxygen species (ROS) levels in RAW264.7 cells were evaluated using 2',7'-dichlorofluorescein diacetate (DCFH-DA) after treated with different formulations. Upon stimulation with LPS, a strong green fluorescence was observed in the cells, indicating the successful induction of oxidative stress in RAW264.7 cells. HA-RM-Cel-BR group showed a superior ROS scavenging ability compared to the groups of free Cel and free BR (Fig. 4b), which can facilitate the reduction of inflammation associated with oxidative stress. Flow cytometry analysis showed the fluorescence intensity in HA-RM-Cel-BR group was significantly reduced (Fig. 4c-d), indicating the significant ROS scavenging ability of HA-RM-Cel-BR.

In addition, the increase of nitric oxide (NO) level is also a hallmark of inflammation-stimulated M1 macrophages. NO can oxidize DNA, proteins, and lipids into autoantigens to trigger an autoimmune response and exacerbate the pathological processes of RA [11, 35]. The intracellular NO levels were detected by cell-permeable fluorescent probe 4-amino-5-methylamino-2',7'-difluorofluorescein diacetate (DAF-FM DA). The results showed that the green fluorescence intensity in macrophages was significantly enhanced after LPS stimulation, while the fluorescence intensity of macrophages was significantly reduced after treatment with Cel-BR and HA-RM-Cel-BR respectively (Fig. 4e-f), indicating that HA-RM-Cel-BR effectively reduced the level of NO, which can help to maintain intracellular redox balance.

HA-RM-Cel-BR induced the polarization of macrophage in vitro

CD86 and CD206 were employed as biomarkers for M1 and M2 macrophages, respectively, to evaluate the ability of HA-RM-Cel-BR to induce macrophage polarization in vitro. The results showed that the level of pro-inflammatory M1-type macrophage marker CD86 was significantly increased in M0 macrophages after LPS stimulation. In contrast, treatment with Cel-BR and HA-RM-Cel-BR resulted in a significant decrease in CD86-positive cells and a substantial increase in CD206-positive cells (Fig. 5a, b), indicating that both Cel-BR and HA-RM-Cel-BR effectively repolarized M1 macrophages to M2 phenotype. Furthermore, the effect of HA-RM-Cel-BR was superior to that of Cel-BR, which may be attributed to the targeting ability of HA.

In addition, the pro-inflammatory cytokines of IL-6 and TNF-α (markers of M1 macrophages) and the inhibitory inflammatory cytokine of IL-10 (markers of M2 macrophages) were detected by ELISA kits. The results showed that HA-RM-Cel-BR significantly reduced the expression levels of TNF-α and IL-6 (Fig. 5e and f), and increased the expression of IL-10 (Fig. 5c), indicating that HA-RM-Cel-BR can regulate the inflammatory microenvironment of RA.

To further investigate the mechanism of macrophage phenotypic change in HA-RM-Cel-BR, Western blot assay was used to evaluate the expression of related pathway proteins. Compared with the control group,

HA-RM-Cel-BR downregulated the expression of STING (Fig. 5d; Figure S14 f), p-NF-κB and p-IκBα (Fig. 5g-h; Figure S14 a, b). In addition, the Nrf-2/HO-1 pathway has been found to enhance cellular antioxidant ability and reduce inflammatory response [36, 37]. The results of Western blotting (WB) analysis showed an upregulation of Nrf-2 expression and downregulation of Keap1 expression after treatment with Cel-BR and HA-RM-Cel-BR. Furthermore, the anti-oxidative stress effector heme oxygenase 1 (HO-1) was also upregulated (Fig. 5i; Figure S14 c-e), suggesting that HA-RM-Cel-BR can effectively activate the antioxidant system.

Based on these experimental results, we speculate that the mechanism by which HA-RM-Cel-BR regulates the repolarization of M1 macrophages to M2 macrophages is the synergistic effect of Cel inhibition on the STING signaling pathway and BR activation on the Nrf2/HO-1 signaling pathway (Fig. 5j), which facilitates to restore normal immune function in the joint.

Transcriptomic analysis of macrophage Immunomodulation by HA-RM-Cel-BR

To further explore the potential therapeutic mechanism of HA-RM-Cel-BR in regulating the immune microenvironment through macrophages, we performed transcriptome sequencing analysis on RAW264.7 cells after stimulated by LPS and then treated with PBS and HA-RM-Cel-BR, respectively. Compared with PBS group, 1248 genes in HA-RM-Cel-BR group were significantly dysregulated, including 761 up-regulated (right, red) and 487 down-regulated (left, blue) genes (Fig. 6a). Principal component analysis (PCA) showed significant separation between PBS treatment group and HA-RM-Cel-BR group (Fig. 6b), indicating that HA-RM-Cel-BR significantly affected macrophage RNA transcription. Pearson correlation coefficient r indicated strong sample repeatability (Fig. 6c), and cluster analysis results were consistent with PCA (Fig. 6d).

Subsequently, gene ontology (GO) analysis was performed for differentially expressed genes (DEGs) associated with HA-RM-Cel-BR and PBS treatment groups (Fig. 6e). The results suggest that HA-RM-Cel-BR plays an immunomodulatory role by regulating cytokine production, cell-cell adhesion, immune effect and adaptive immune responses. In addition, KEGG pathway enrichment analysis of differentially expressed genes (DEGs) showed that the down-regulated genes were involved in cytokine/cytokine receptor interactions, NF-κB signaling pathway, IL-17 signaling pathway, MAPK signaling pathway, and cytosolic DNA sensing pathway (Fig. 6f). The involvement of cytosolic DNA-sensing pathway indicated that the activation of STING signaling pathway could be further inhibited after HA-RM-Cel-BR treatment. Collectively, HA-RM-Cel-BR maintains the immune balance of the inflammatory microenvironment through multiple signaling pathways and biological process regulation.

Evaluation of HA-RM-Cel-BR targeting in vivo

DIR (1,1'-Dioctadecyl-3,3,3',3'-tetramethylindotricarbocyanine iodine) was employed as a fluorescent dye to label nanomedicines to investigate their joint targeting in vivo. The results showed that the accumulation of HA-RM-Cel-BR@DIR in the ankle joint was significantly greater than that of free DIR and Cel-BR@DIR at different time points (Fig. 7a). The fluorescence analysis of isolated organs showed that the accumulation of HA-RM-Cel-BR@DIR in the inflamed joints was significantly higher than that of either free DIR or Cel-BR@DIR (Fig. 7b). These results indicated that RM encapsulation and DSPE-PEG-HA modification enhanced the targeting ability of HA-RM-Cel-BR to RA lesions. That is to say, the overexpression of CD44 receptor and activation of inflammatory endocytosis pathway enhanced the active targeted uptake of HA-RM-Cel-BR [35], while the vascular leakage and lymphatic drainage disorders driven by inflammatory factors promoted the passive accumulation of HA-RM-Cel-BR in RA-inflected joints [38].

Therapeutic effect of HA-RM-Cel-BR on RA in vivo

The effects of different formulations on RA were evaluated in an adjuvant-induced arthritis (AIA) model, administered through the tail vein for a total of five treatments (Fig. 8a). The results showed that Cel-BR and HA-RM-Cel-BR treatment groups significantly reduced joint swelling, fever, and functional scores, compared with other treatment groups (Fig. 8b-f). Notably, HA-RM-Cel-BR showed the highest therapeutic efficacy, which may be attributed to RM encapsulation prolonged blood circulation and HA modification enhanced the targeting to RA.

Because bone erosion is a prominent symptom of RA, we evaluated the extent of bone erosion in RA rats using micro-computed tomography (micro-CT) (Fig. 8g). The CT scans of the hind paws from the model group showed significant bone erosion and deformation (rough surface or abnormal trabecular structure, as indicated by red arrows), which is consistent with clinical reports of arthritis-induced bone damage [39]. However, the bone erosion was significantly inhibited after treatment with HA-RM-Cel-BR, with only negligible surface erosion. After treatment, the walking tracks of rats in different groups were recorded. The results showed that Cel-BR and HA-RM-Cel-BR significantly improved the walking function and reduced the swelling of joints of RA rats (videos S1-S6: Control, Model, Free Cel, Free BR, Cel-BR, HA-RM-Cel-BR). Notably, the therapeutic effect of Cel-BR was superior to that of Free Cel and Free BR, which

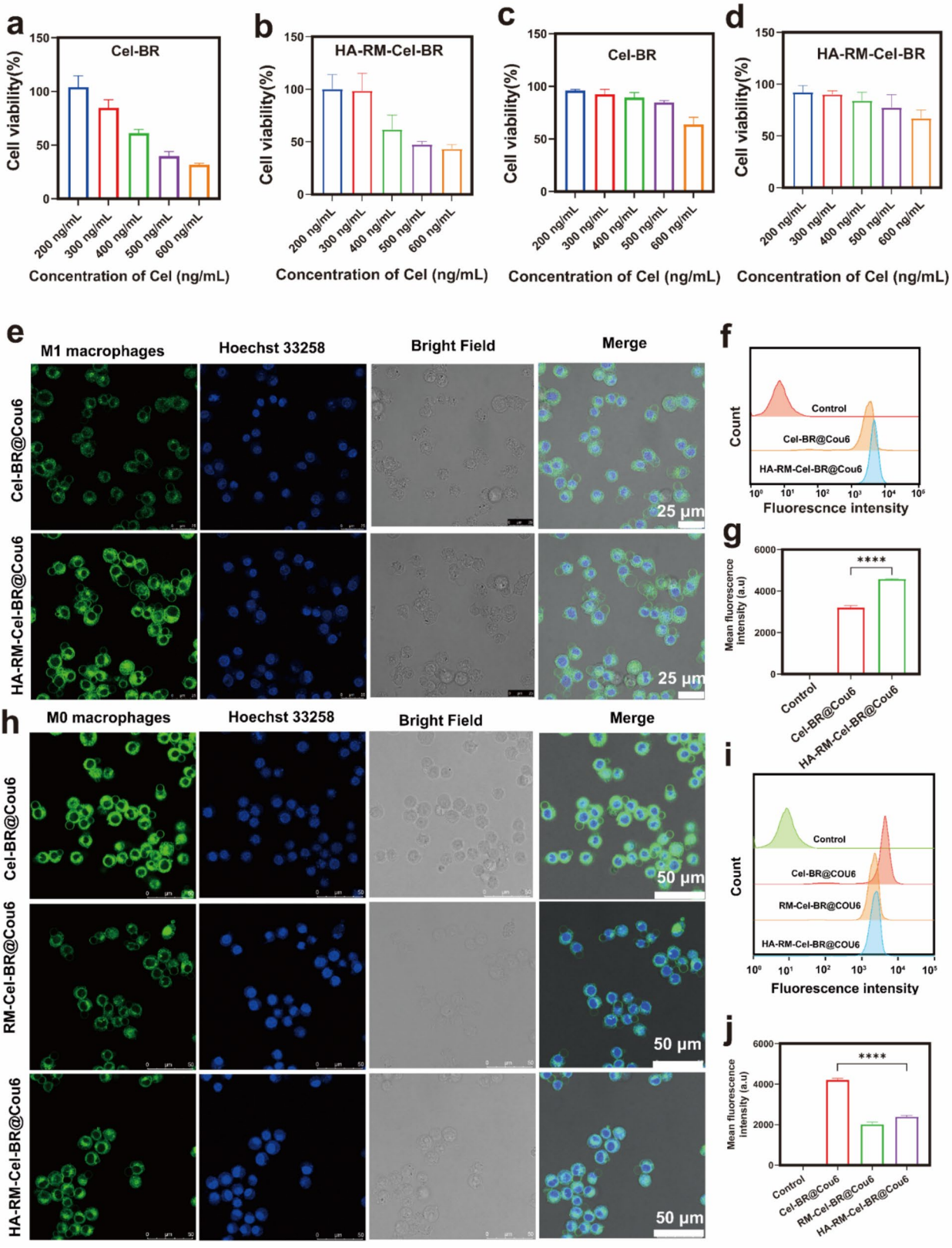

Fig. 3 Biocompatibility and targeting evaluation of HA-RM-Cel-BR in vitro. Cytotoxicity of Cel-BR (**a**) and HA-RM-Cel-BR (**b**) on RAW264.7 cells. Cytotoxicity of Cel-BR (**c**) and HA-RM-Cel-BR (**d**) on FLS cells. Fluorescence images (**e**), flow cytometry count (**f**) and mean fluorescence (**g**) of HA-RM-Cel-BR on LPS-treated macrophages (M1 macrophages), scale bar = 25 μm. Fluorescence images (**h**) flow cytometry count (**i**) and mean fluorescence (**j**) of HA-RM-Cel-BR on LPS-untreated macrophages (M0 macrophages), scale bar = 50 μm. Data are presented as mean ± SD ($n = 3$). *$P < 0.05$, **$P < 0.01$, and ***$P < 0.001$

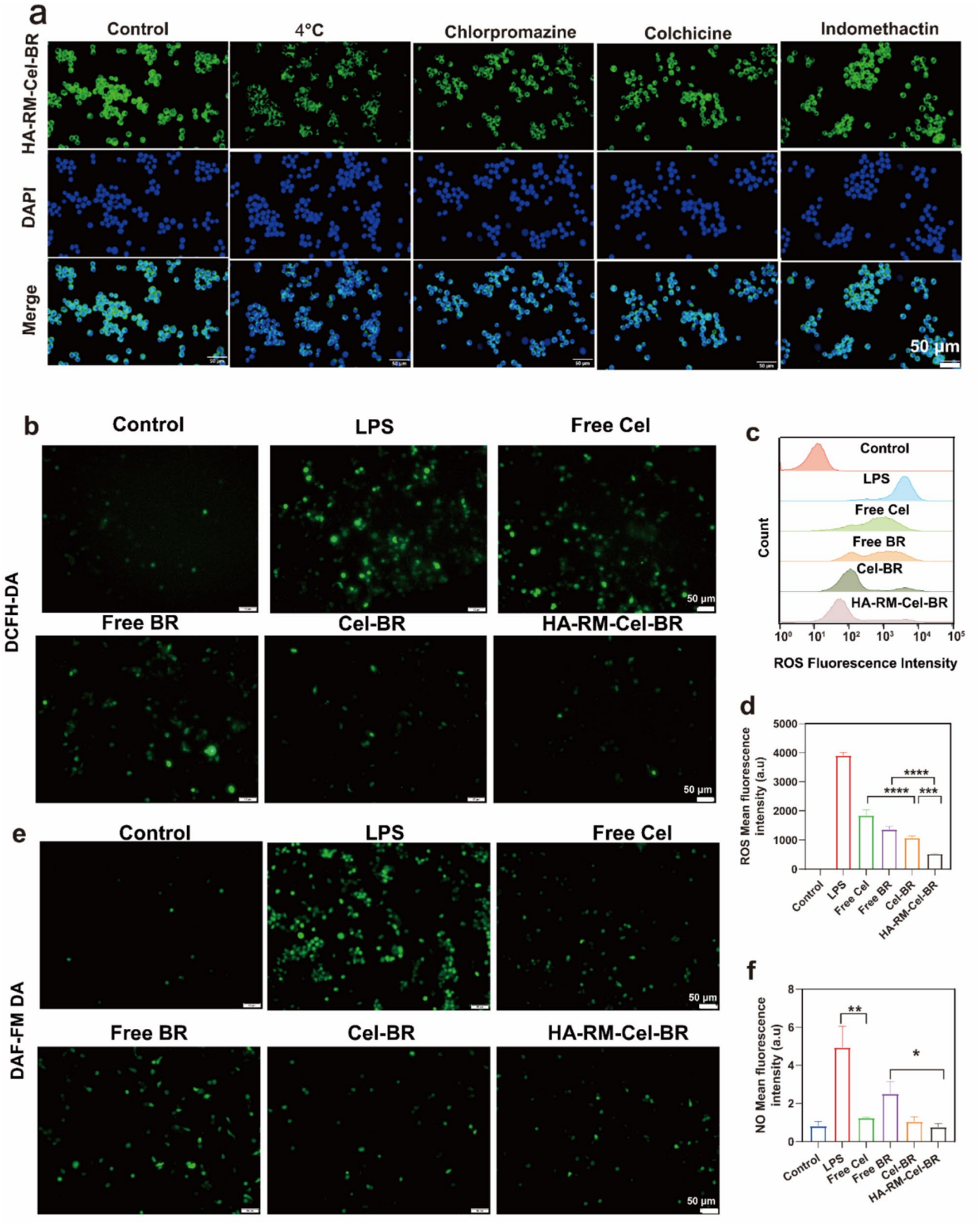

Fig. 4 Evaluation of the mechanism of HA-RM-Cel-BR cell internalization and clearance of ROS and NO *in vitro*. (**a**) Images of HA-RM-Cel-BR cellular uptake after treatment with different inhibitors (chlorpromazine, colchicine, indomethacin) or 4℃. Scale bar = 50 μm. (**b**-**d**) Fluorescence images and flow cytometry quantification of intracellular ROS levels in RAW 264.7 cells cultured with free Cel, free BR, Cel-BR, and HA-RM-Cel-BR, scale bar = 50 μm. (**e**-**f**) Fluorescence images and fluorescence quantification of intracellular NO levels in RAW 264.7 cells cultured with free Cel, free BR, Cel-BR, and HA-RM-Cel-BR, scale bar = 50 μm. Data are expressed as mean ± SD ($n = 3$). $^{*}P < 0.05$, $^{**}P < 0.01$, and $^{***}P < 0.001$

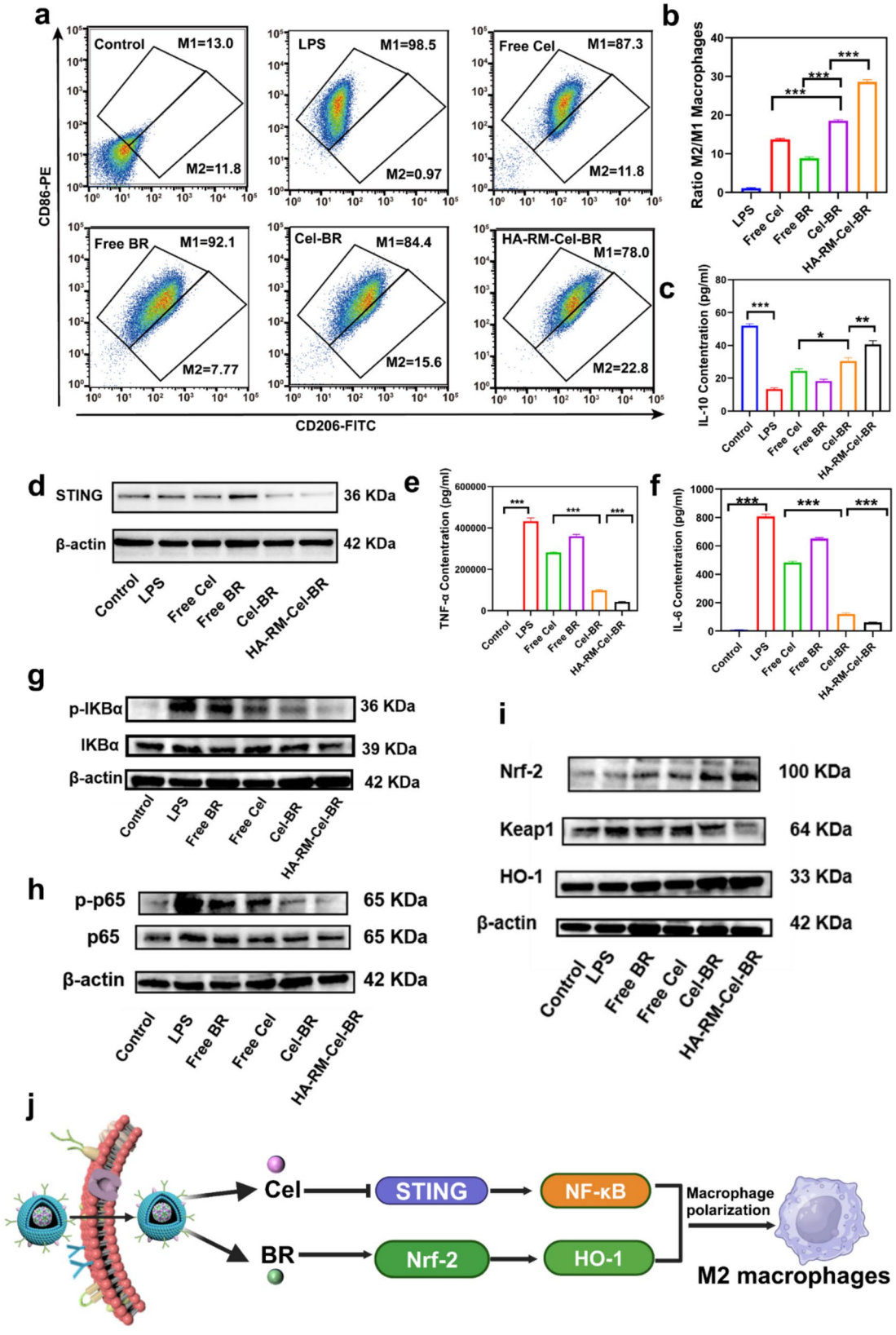

Fig. 5 (See legend on next page.)

(See figure on previous page.)

Fig. 5 Regulation and mechanism of M2 macrophage polarization by HA-RM-Cel-BR in vitro. Flow cytometry analysis of CD86 and CD206 expression levels (**a**) and relative expression of M2 macrophages (**b**) after different treatments. ELISA assay quantification of IL-10 (**c**), TNF-α (**e**), and IL-6 (**f**) expression levels in different formulation groups. (**d**) Protein expression levels of STING in RAW 264.7 cells after treatment with different formulations. Protein expression levels of p-IκBα, IκBα (**g**), p-p65, and p65 (**h**) in RAW 264.7 cells after treatment with different formulations. (**i**) Protein expression levels of Nrf-2, Keap1, and HO-1 in RAW 264.7 cells after treatment with different formulations. (**j**) Mechanism diagram of HA-RM-Cel-BR regulates macrophage polarization. Data are presented as mean ± SD ($n = 3$). *$P < 0.05$, **$P < 0.01$, and ***$P < 0.001$

further proves the synergistic therapeutic effect of Cel and BR.

Hematoxylin and eosin (H&E) staining of the ankle joint tissue in the model, Free Cel and Free BR groups showed significant inflammatory cell infiltration, severe hyperplastic synovial tissue, bone erosion, and infiltration of vascular opacified tissue in the joint cavity. In contrast, after treatment with Cel-BR and HA-RM-Cel-BR, the joint lesions were significantly improved, with only slight inflammatory cell infiltration was observed, and the bone morphology was intact and similar to the normal group (Fig. 9a). In addition, the extent of cartilage damage after treated with different formulations was evaluated by Senna O-Fixed Green (SO-FG) staining. The results showed that the cartilage structure in the model group was significantly destroyed, while the cartilage treated by HA-RM-Cel-BR was close to the level of the normal group. Moreover, the cartilage recovery was not significant in the Free Cel (1 mg/kg) and Free BR (20 mg/kg) groups at the equivalent doses of Cel-BR (Fig. 9b), indicating that the combination of Cel and BR exerts a significant inflammatory inhibitory effect.

HA-RM-Cel-BR remodels the inflammatory immune microenvironment in vivo

M1 macrophages play a crucial role in regulating inflammation and tissue destruction, which affects the onset and progression of RA. Therefore, the ability of HA-RM-Cel-BR to regulate macrophage polarization and remodel the immune microenvironment in vivo was evaluated by immunofluorescence. ELISA results showed that the expression of tumor necrosis factor-alpha (TNF-α) and interleukin-6 (IL-6) cytokine in serum was significantly down-regulated, indicating that HA-RM-Cel-BR effectively reduced the secretion of inflammatory factors from M1 macrophages (Fig. 9g-h). Immunohistochemical analysis of the ankle joint confirmed that HA-RM-Cel-BR effectively reduced the inflammatory infiltration of TNF-α and IL-6 (Fig. 9e, f).

In addition, the number of osteoclasts and osteoblasts was evaluated by acid phosphatase anti-tartaric acid staining (TRAP staining) and alkaline phosphatase staining (ALP staining) (Fig. 9c, d). The results showed that the number of TRAP-positive cells decreased significantly while the number of ALP-positive cells increased significantly after HA-RM-Cel-BR treatment. These results also explain why almost no bone erosion was observed after HA-RM-Cel-BR treatment.

The changes of immune cells in joints can be observed more clearly by immunofluorescence staining. The results showed that the proportion of M1 macrophages was significantly reduced (INOS, red), while the proportion of M2 macrophages was significantly increased (CD206, green) (Fig. 10a, d, e). To more intuitively verify the polarization effect of HA-RM-Cel-BR in the tissue microenvironment, immunohistochemistry was used to detect the co-localization of M1 (CD86) and M2 (CD206) macrophage markers. The results showed that the expression of CD206 in HA-RM-Cel-BR group significantly increased, while the expression of CD86 decreased (Figure S19), indicating that HA-RM-Cel-BR induced the polarization of macrophages towards M2 phenotype. These results confirm the ability of HA-RM-Cel-BR to regulate the polarization of M1 macrophages to M2 macrophages in vivo, which is consistent with the results of previous cellular experiments.

The evaluation of immune cell expression in the ankle joint showed that a significant increase in Treg cells (FOXP3, green) (Fig. 10b, f), and a notable decrease in Th17 cells (IL-17, red) after HA-RM-Cel-BR treatment (Fig. 10b, g). These results indicate that HA-RM-Cel-BR can effectively regulate the immune balance of the joint microenvironment to inhibit the progression of inflammation. In addition, the excessive production of plasma cells in RA can promote differentiation of osteoclasts and lead to bone erosion. The results of immunofluorescence staining (Fig. 10c, h) showed that HA-RM-Cel-BR significantly downregulated plasma cell expression (CD138, yellow). Consequently, HA-RM-Cel-BR remodels the inflammatory microenvironment of RA by inducing M2 macrophage polarization, which is conducive to promoting the healing of injured joints (Fig. 10i).

Evaluation of HA-RM-Cel-BR for reducing toxicity in vivo

To evaluate the biocompatibility and biosafety of HA-RM-Cel-BR, we conducted histopathological analyses of the major organs in rats. H&E staining showed no significant damage to the heart, spleen, lungs, or kidneys across all treatment groups (Figure S15), and there were no significant changes in the body weight in all groups (Fig. 9i). In addition, the results of hemolysis test showed that no red blood cell disruption was observed after Cel-BR and HA-RM-Cel-BR treatment, and the optical density (OD)

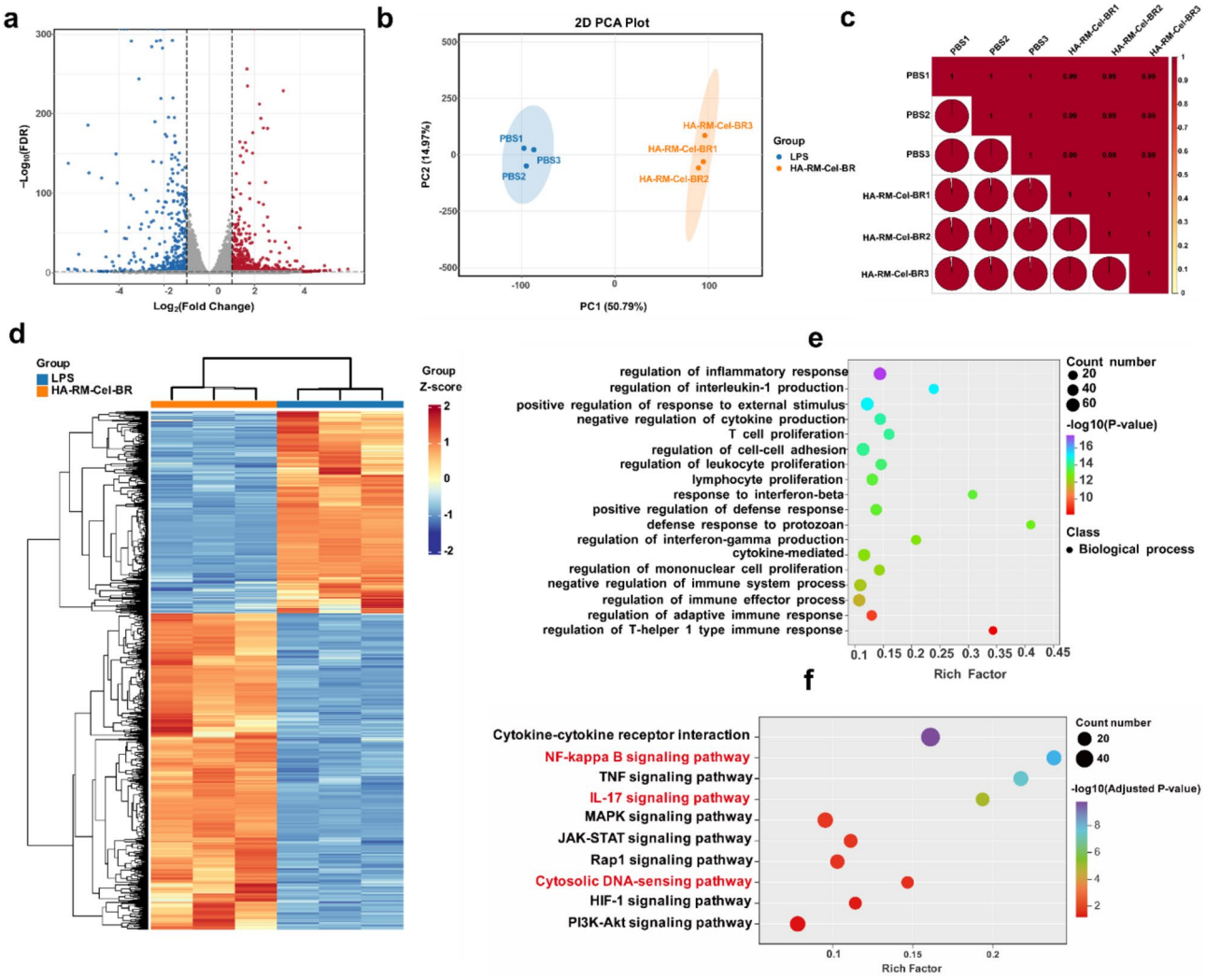

Fig. 6 Transcriptomic analysis of macrophage immunomodulation by HA-RM-Cel-BR. (**a**) Volcano plot of differentially expressed genes in RAW 264.7 between PBS and HA-RM-Cel-BR treated groups. (**b**) Principal component analysis (PCA) in RAW 264.7 between PBS group and HA-RM-Cel-BR treatment. (**c**) Pearson's correlation coefficient r to verify sample reproducibility. (**d**) Heat map of the DEGs related to inflammation and immune regulation. (**e**) GO enrichment term analysed for its effect on macrophage function. (**f**) KEGG pathway enrichment analysis ($P < 0.05$)

values at 545 nm were close to that of the negative control (Figure S18), indicating their good blood compatibility.

Given that Free Cel has been associated with specific toxic effects on the liver, we specifically evaluated the hepatotoxicity of different formulations. H&E staining of the liver showed that cellular crumpling and damage of liver tissue were observed in rats in the Free Cel group at the end of treatment (Figure S16), while no significant liver damage was observed in the Cel-BR and HA-RM-Cel-BR groups. Immunohistochemical assays showed an increased expression of TNF-α and IL-6 in the liver of rats in the Free Cel group, while no significant increase in the Cel-BR and HA-RM-Cel-BR groups (Figure S17). Furthermore, blood chemistry tests showed that alanine aminotransferase (ALT), alkaline phosphatase (ALP), and aspartate aminotransferase (AST) levels were significantly increased in the Free Cel group (Fig. 9j-l), indicating a certain degree of liver injury. Fortunately, there was no significant increase after Cel-BR and HA-RM-Cel-BR treatments, which further confirms that the combination of Cel and BR significantly mitigated liver injury. These results indicate that HA-RM-Cel-BR has favorable biosafety in vivo, and significantly reduces the hepatotoxicity of Cel.

Discussion and prospects

Based on the TCM theory, we developed a biomimetic nanomedicine HA-RM-Cel-BR, which realized the effective treatment of RA and mitigated the liver toxicity associated with Cel (Fig. 11). To our knowledge, this is the first study on the co-assembly of TCM active ingredient Cel and BR for RA treatment, which helps to promote the

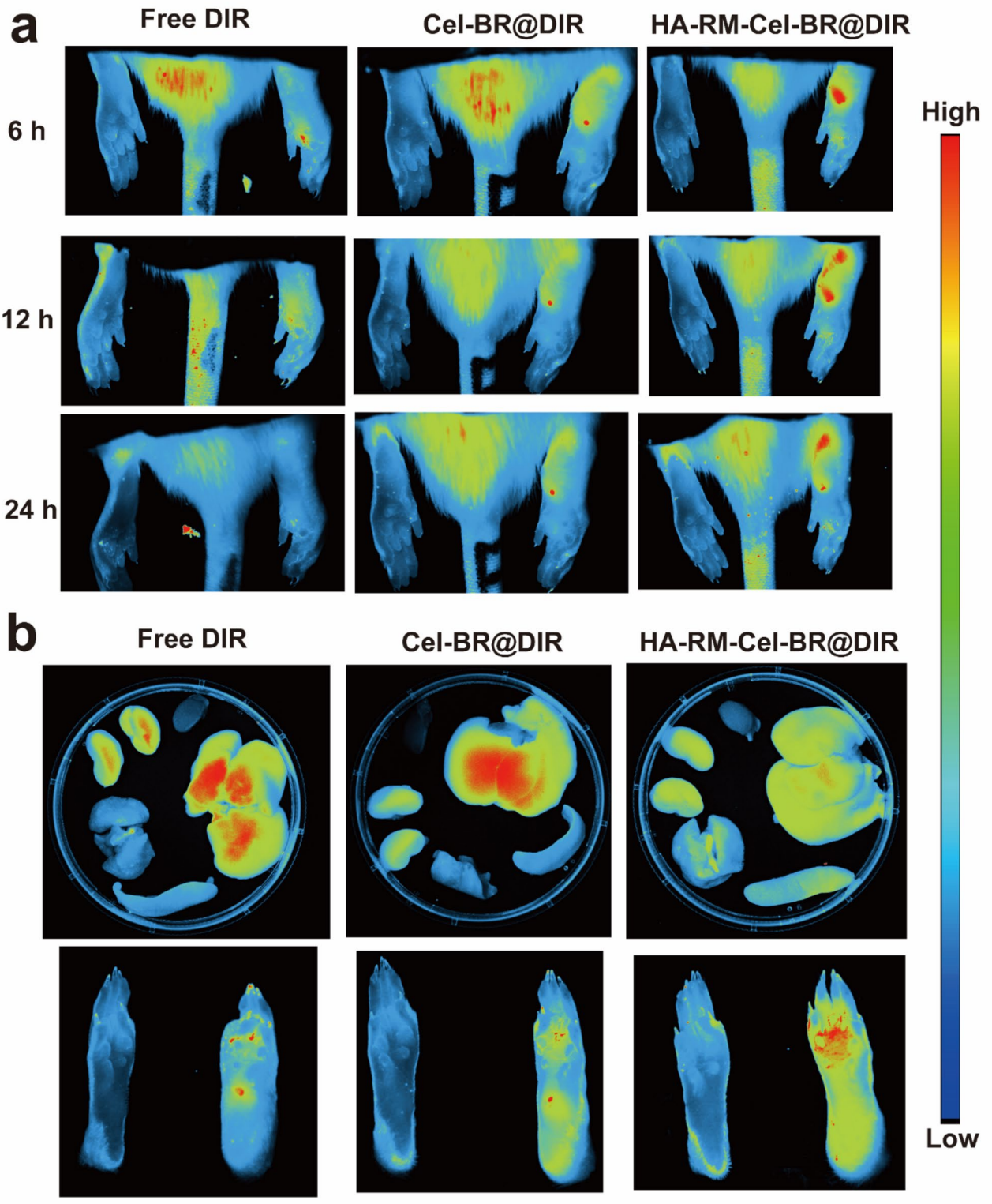

Fig. 7 Evaluation of HA-RM-Cel-BR targeting in vivo. In vivo fluorescence imaging of the joints at different time points after intravenous injection of Free DIR, Cel-BR@DIR, and HA-RM-Cel-BR@DIR (**a**), and ex vivo fluorescence distribution in heart, liver, spleen, lungs, kidneys, and joints (**b**)

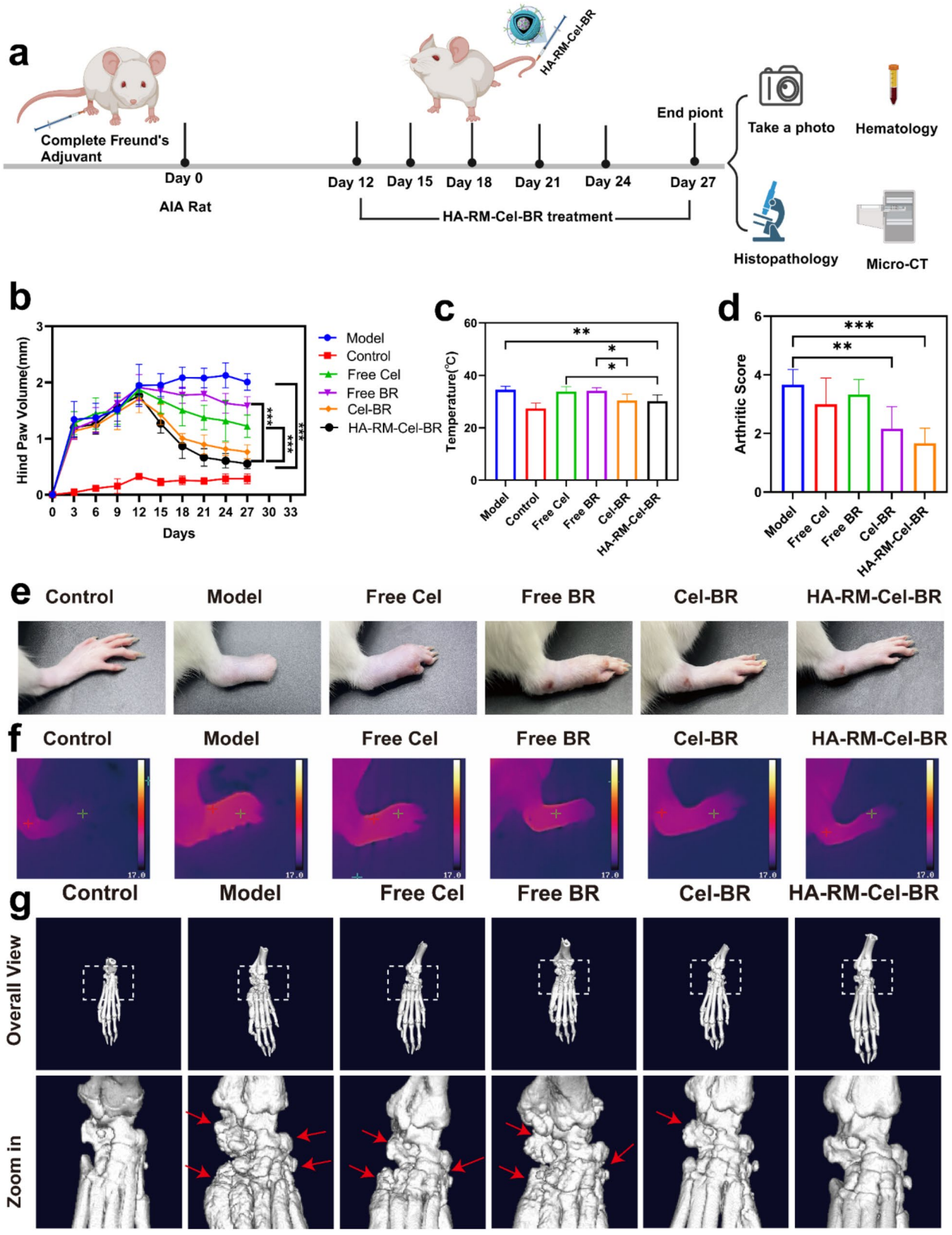

Fig. 8 Therapeutic effect of HA-RM-Cel-BR on RA in vivo. (**a**) Establishment and treatment protocol of RA rat model. (**b**) Degree of toe swelling in different treatment groups. (**c**, **f**) Temperatures of inflamed paws measured by thermal imaging. (**d**) Arthritis function score in different treatment groups. (**e**) Photographs of inflamed joints in different treatment groups. (**g**) Micro-computed tomography (micro-CT) analysis of bone tissues in different treatment groups. Data are presented as mean ± SD ($n = 6$). *$P < 0.05$, **$P < 0.01$, and ***$P < 0.001$

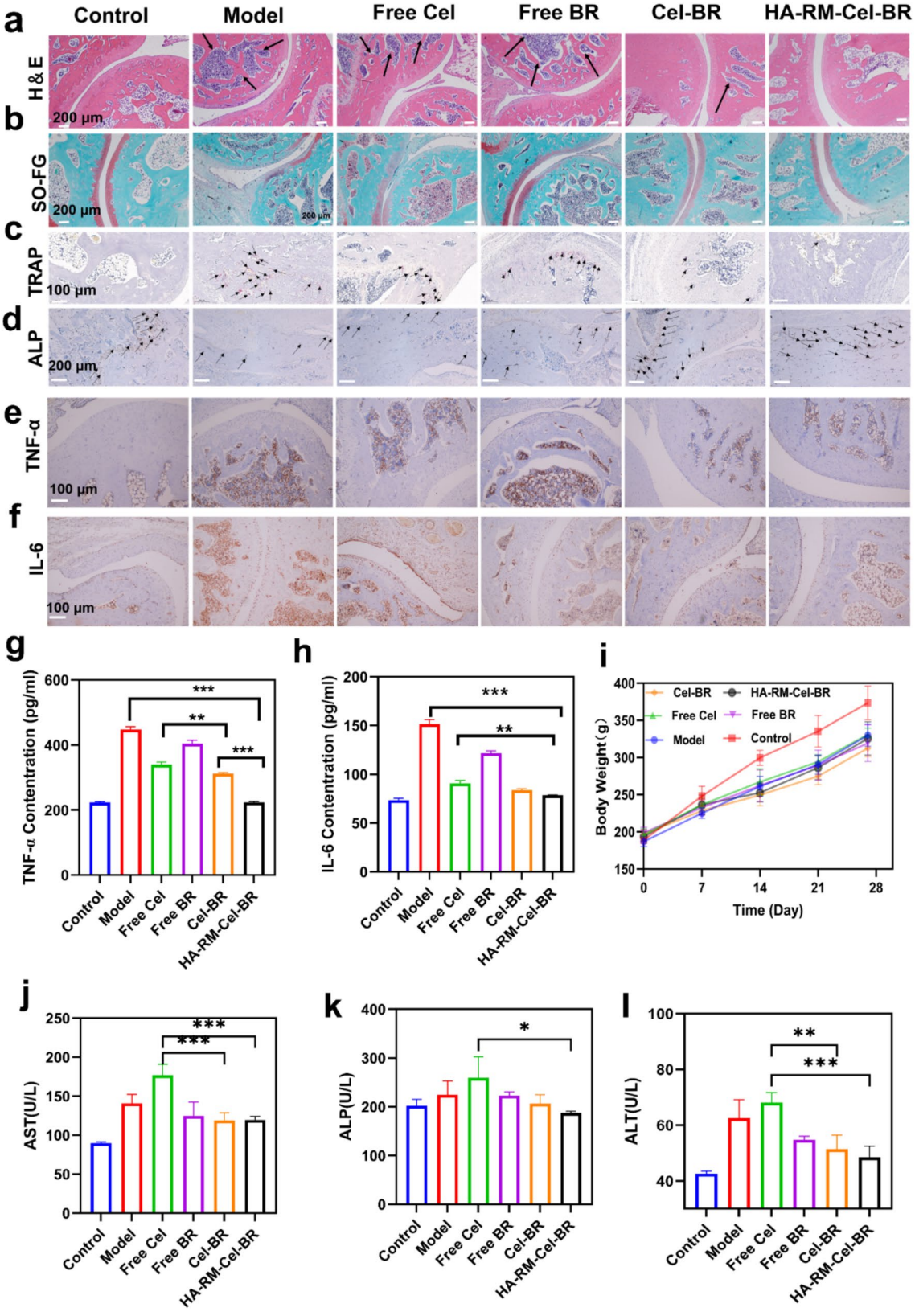

Fig. 9 (See legend on next page.)

(See figure on previous page.)

Fig. 9 Staining and immuno-histochemical analysis of ankle joint tissue. (**a**) Representative H&E-stained sections of the joints from different groups. Inflammatory cell infiltration indicated by black arrows, scale bar = 200 μm. (**b**) Representative sections of the joints stained with Safranin O-Fast Green from different groups, scale bar = 200 μm. Expression levels of TRAP-stained osteoclasts (**c**) and ALP-stained osteoblasts (**d**) in the joints from different groups, scale bar = 100 μm and 200 μm. Immuno-histochemical analysis of TNF-α (**e**) and IL-6 expression levels in ankle joints from different groups (**f**), scale bar = 100 μm. ELISA analysis of TNF-α (**g**) and IL-6 cytokine levels (**h**) in blood samples from different groups. (**i**) Weight changes after treatment with different formulations. Levels of AST (**j**), ALP (**k**), and ALT (**l**) in serum samples. Data are presented as mean ± SD ($n = 3$). *$P < 0.05$, **0.01, and ***$P < 0.001$

development of nanomedicines based on TCM theory. Compared to previously reported drugs for RA treatment, the advantages of HA-RM-Cel-BR are as follows:

(1) In recent years, an increasing number of studies have shown that abnormal activation of cGAS-STING signaling pathway and increase of autoantigens caused by RONS are important reasons for the difficulty in RA. However, relatively few studies have focused on the dual strategy of inhibiting STING and removing RONS. Inspired by TCM theory, we constructed a biomimetic nano-Chinese medicine system HA-RM-Cel-BR based on the STING inhibition of Cel and the RONS clearance of BR. HA-RM-Cel-BR effectively regulates the immune microenvironment of RA and restore the normal structure and function of joints.

(2) Previously reported delivery of RA treatments, such as Leflunomide [40] and dexamethasone [41], required the complex synthesis of nanocarriers, which suffer from drug side effects and potential toxicity of the carriers. Moreover, the immune balance of RA microenvironment was not improved to prevent continued joint destruction [42, 43]. In contrast, our carrier-free drug delivery system HA-RM-Cel-BR, not only effectively inhibited the ongoing RA inflammation by regulating the immune balance of RA microenvironment, but also avoided the potential toxicity of the carriers.

(3) HA-RM-Cel-BR was constructed based on the combination of TCM theory and modern drug delivery technology. The blood circulation of HA-RM-Cel-BR was prolonged by RM encapsulation, and its targeting to RA was enhanced by HA modification. HA-RM-Cel-BR can maintain the immune balance of the inflammatory microenvironment through multiple signaling pathways and biological process regulation, such as STING, IL-17, MAPK signaling pathways (Fig. 6f). Importantly, HA-RM-Cel-BR has the advantages of simple preparation, high drug loading capacity and low toxicity, and is expected to achieve clinical transformation.

(4) When Free Cel is used alone, it has significant side effects such as liver toxicity in vivo. Through carrier-free self-assembly of BR and Cel, we not only avoid the toxic side effects on liver, but also realize the synergistic treatment of RA to improve the therapeutic efficacy.

Recent studies have found that overexpression of hydrogen peroxide in the inflammatory microenvironment can promote the in-situ conversion of BR into biliverdin, which has excellent photothermal conversion performance [44]. Based on this molecular transformation mechanism, we speculate that the combination of HA-RM-Cel-BR and photothermal therapy (PTT) is expected to achieve better therapeutic effects [45, 46]. In addition, HA-RM-Cel-BR has the advantages of simple preparation process, high drug loading and good biocompatibility, which has great potential in clinical transformation.

However, there are still limitations to our study. The efficacy of HA-RM-Cel-BR needs to be verified by more comprehensive preclinical studies, especially its long-term safety and pharmacokinetic properties, which are critical to evaluate its clinical application value. The long-term immunomodulatory effects of HA-RM-Cel-BR in vivo still need to be further explored. In the future study, the active ingredients of Chinese medicine can be combined with methotrexate, sulfasalazine, and other first-line treatment drugs to reduce the side effects of single drug use and enhance the efficacy of RA, providing more effective and safe treatment options for RA patients.

Conclusion

A biomimetic nano-Chinese medicine (HA-RM-Cel-BR) is developed through the carrier-free self-assembly of Cel and BR, which based on the combination of TCM theory with modern drug delivery technology. By inhibiting STING pathway and eliminating RONS, HA-RM-Cel-BR effectively alleviates joint inflammation and bone erosion, and restores the normal function of joints. More importantly, HA-RM-Cel-BR effectively reduced hepatotoxicity associated with Cel and showed promising clinical translation potential.

Materials and methods

Materials

Bilirubin (BR) was purchased from Aladdin Biochemical Technology Co., Ltd. (Shanghai, China). Celastrol (Cel) extract was obtained from Maclyn Biochemical Technology Co., Ltd. (Shanghai, China). Coumarin 6 (Cou6) was purchased from Aladdin Biochemical Technology Co., Ltd. (Shanghai, China). DSPE-PEG_{2000}-HA was purchased

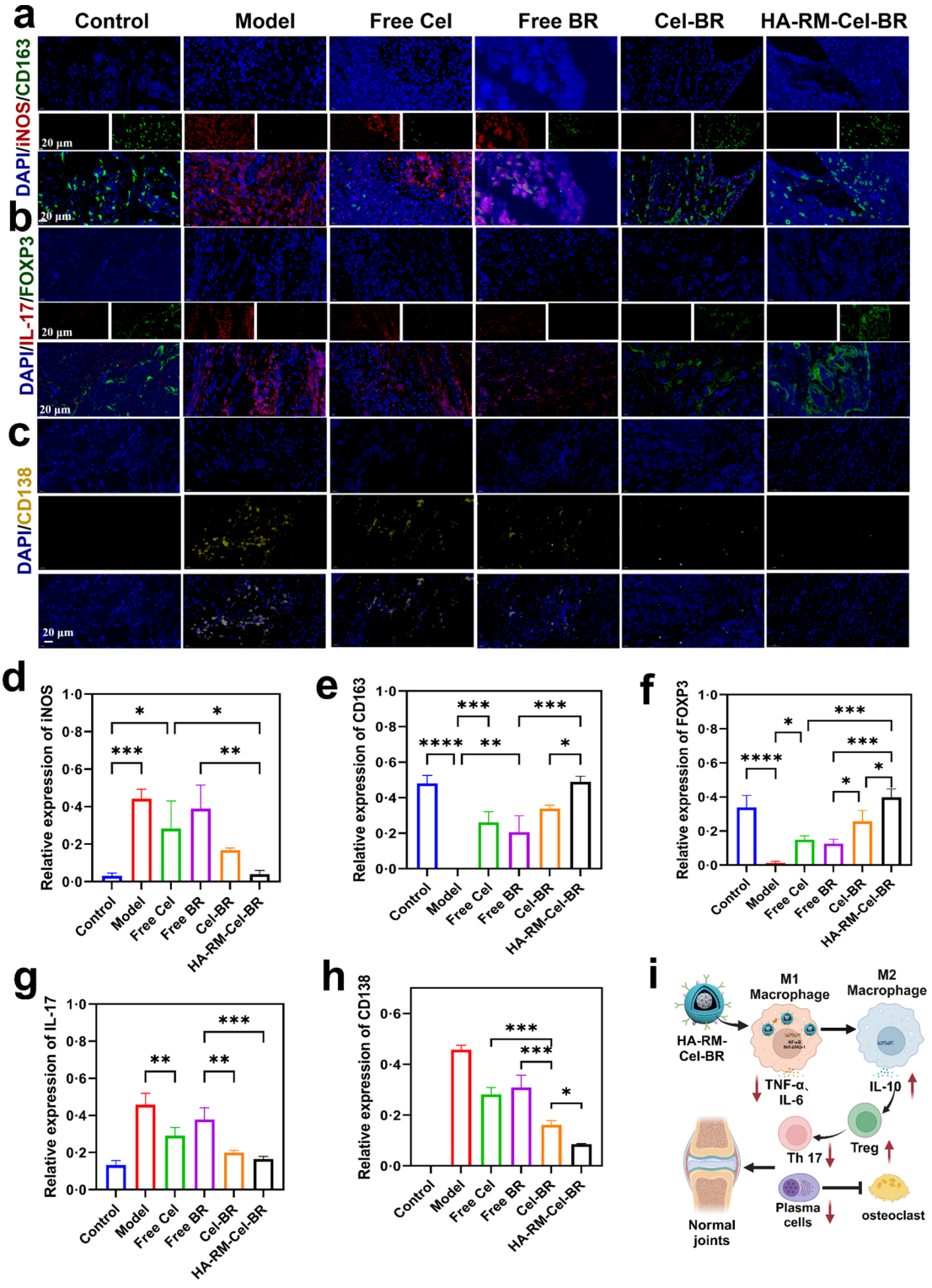

Fig. 10 Reshaping of RA immune microenvironment by HA-RM-Cel-BR. (**a**) Immunofluorescence staining of M1 macrophages (iNOS: red) and M2 macrophages (CD163: green) in ankle joints, scale bar = 20 μm. (**b**) Immunofluorescence of Treg cells (FOXP3: green) and Th17 cells (IL-17: red) in ankle joints. (**c**) Immunofluorescence expression of plasma cells (CD138: yellow) in ankle joints. Relative expression levels of iNOS (**d**), CD163 (**e**), FOXP3 (**f**), IL-17 (**g**), and CD138 (**h**) in ankle joints. (**i**) Schematic representation of HA-RM-Cel-BR regulating the joint immune microenvironment. Data are presented as mean ± SD ($n = 3$). *$P < 0.05$, **$P < 0.01$, and ***$P < 0.001$

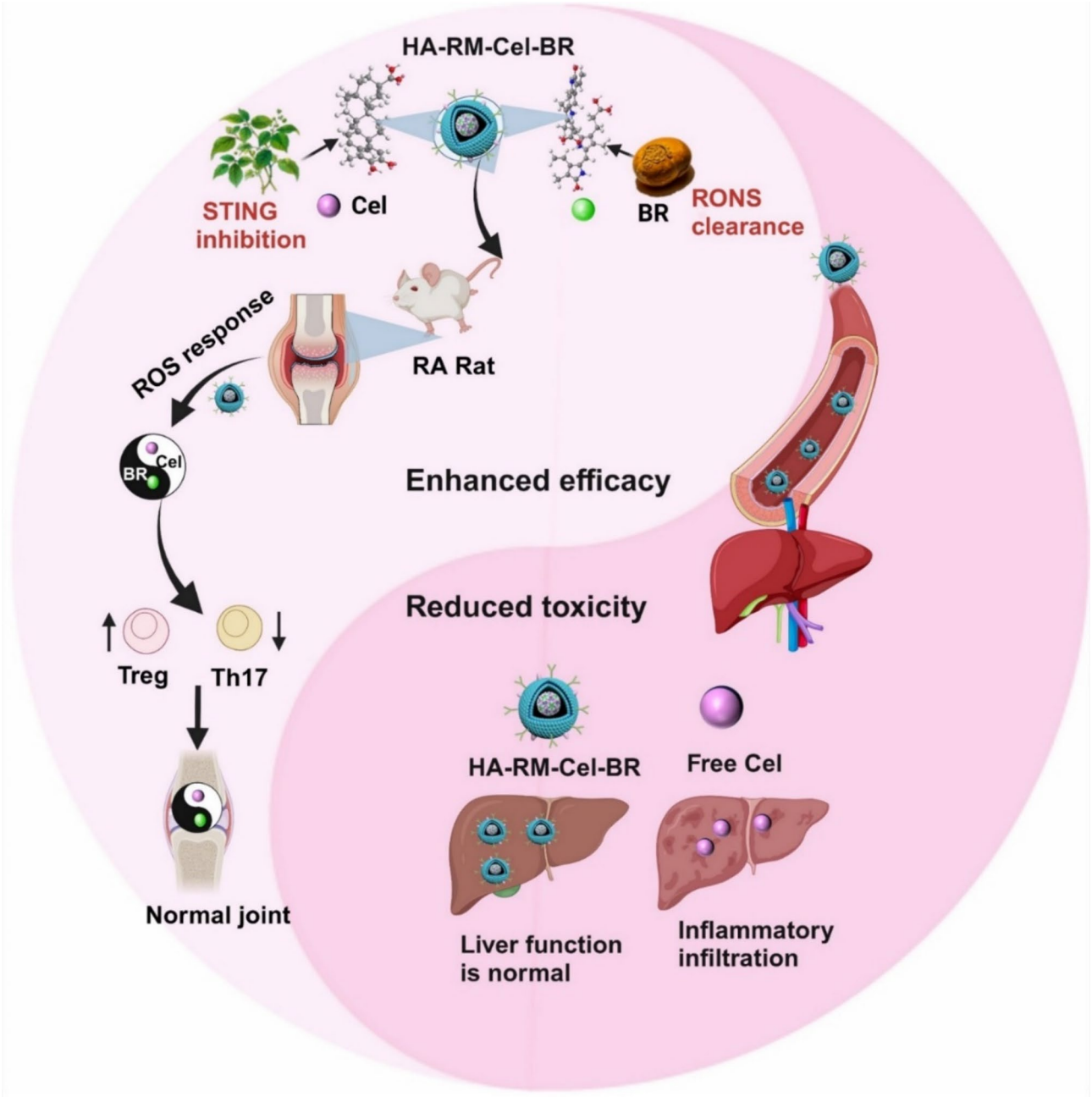

Fig. 11 Schematic representation of HA-RM-Cel-BR synergistically enhancing efficacy and reducing toxicity. Synergistic effects of Cel and BR regulate the RA immune microenvironment to achieve joint repair (left). Synergy between BR and Cel reduces hepatotoxicity associated with Cel (right). Created with www.BioRender.com

from Yusi Pharmaceutical Technology Co., Ltd (Chongqing, China). Complete Freund's adjuvant was purchased from Chondrex (USA, Washington). Anti-CD86-PE and anti-CD206-FITC were purchased from Thermo Fisher Scientific. Lipopolysaccharide (LPS) was purchased from Solabio Life Sciences Co., Ltd. (Beijing, China). Interleukin-4 (IL-4,Cat#CK15) was purchased from Novoprotein Scientific Inc Co., Ltd. (Shanghai, China). 1,1'-Dioctadecyl-3,3,3',3'-Tetramethylindocarbocyanine Iodide (DIR) was purchased from Yeasen Biotechnology Co., Ltd. (Shanghai, China).

Enzyme-linked immunosorbent assay kits (ELISA) for tumor necrosis factor-alpha (TNF-α), interleukin-6 (IL-6), and interleukin-10 (IL-10) were purchased from Jianglai Biotechnology Co., Ltd. (Shanghai, China). Cell Counting Kit-8 (CCK-8) was purchased from Beyotime Biotechnology (Beijing, China). DCFH-DA and DAF-FM-DA were purchased from Beyotime Biotechnology

Co., Ltd. Primary antibodies against NF-κB, IKB-α, p-NF-κB, p-IKB-α, Nrf-2, Keap1, HO-1, and β-Actin were purchased from ZEN-BIOSCIENCE Co., Ltd. (Chengdu, China). Ultra-sensitive chemiluminescence detection kits, dual-color pre-stained protein markers, and BCA protein quantification kits were purchased from Epizyme Biomedical Technology Co., Ltd. (Shanghai, China). The cDNA libraries were sequenced on the DNB sequencing platform by Metware Biotechnology Co., Ltd. (Wuhan, China). Mouse mononuclear macrophage leukemia cells (RAW264.7 cells), DMEM culture medium, and fetal bovine serum were purchased from Puno Science Co., Ltd. (China). SD rats (160–180 g) were purchased from Jinan Pengyue Experimental Animal Breeding Co., Ltd (Standard No. 370726230101689616).

Preparation of Cel-BR

Cel-BR was prepared using a nanoprecipitation method. Briefly, Cel (10 mg) and BR (20 mg) were dissolved in 2 mL of dimethyl sulfoxide. Cel and BR were mixed according to different mass ratios (1:10, 1:15, 1:20, w/w), and then added drop by drop into deionized water solution. After stirring at 1000 rpm for 10 min, dialysis was performed in a dialysis bag (2000 Da) to obtain Cel-BR.

Extraction of RM

Blood was collected from the hearts of SD rats and centrifuged at 4 °C at 3500 rpm for 20 min to separate the serum and leukocyte layers. The red blood cells were washed by adding an isotonic phosphate buffer solution (PBS), followed by the addition of 0.25× hypotonic PBS, and gently mixed. After being incubated at 4 °C for 20 min, the red blood cells were centrifuged at 10,000 rpm for 15 min to obtain pale pink red blood cell membranes. These membranes were sequentially extruded through 800 nm, 400 nm, and 200 nm polycarbonate membranes, and stored at -80 °C.

Preparation of RM-Cel-BR and HA-RM-Cel-BR

Red blood cell membranes (RM) and Cel-BR nanoparticles were mixed in a mass ratio (w/w) of 1:2. Subsequently, RM-Cel-BR was prepared by sequentially extruding through 800 nm and 400 nm polycarbonate membranes using a liposome extruder. According to the method described previously [47], DSPE-PEG2000-HA (100 μL, 5 mg/mL) was combined with RM-Cel-BR nanoparticles (containing 1 mg/mL of Cel-BR) by magnetic stirring at 500 rpm for 1 h at 37 °C. To prepare Cel-BR@Cou6, an appropriate amount of Cou6 was added to the dimethyl sulfoxide solution of Cel and BR in a similar manner to HA-RM-Cel-BR@Cou6.

Molecular dynamics simulation

Molecular dynamics simulations were conducted using the improved method outlined in reference [48]. The cubic box had a side length of 9 nm, and the simulation system was randomly populated with Cel and BR molecules. The system underwent 50,000 steps of energy minimization, followed by 100 ps of NVT (canonical ensemble) and NPT (isothermal-isobaric ensemble) simulations based on the energy-minimized configuration.

Characterization of Cel-BR and HA-RM-Cel-BR

The size distribution, particle size, and zeta potential of Cel-BR and HA-RM-Cel-BR were determined using a Zetasizer Nano (Malvern Panalytical, UK). The morphology of Cel-BR and HA-RM-Cel-BR was examined using Transmission Electron Microscopy (TEM) (JEM, JEOL, Japan). The interaction between Cel and BR was investigated employing Ultraviolet-Visible Spectrophotometry (UV-vis) and Fourier Transform Infrared Spectroscopy (FT-IR).

Drug release behavior of HA-RM-Cel-BR

HA-RM-Cel-BR was placed in a 2000 Da dialysis bag and placed in a PBS solution (pH = 7.4, 20 mL) containing 0.5% Tween 80 (with or without 10 mmol/L hydrogen peroxide). The dialysis bags were incubated in a thermostatic oscillator (37 °C, 100 rpm), and 1 mL was sampled at set time points, and then supplemented with 1 mL of the original release medium. The concentration of Cel in the samples was determined by high-performance liquid chromatography (Agilent Technologies, Wilmington, DE), and then the cumulative release was calculated.

Cell viability

RAW264.7 cells were inoculated into 96-well plates at a density of 1×10^4 cells per well and incubated in a cell culture incubator for 12 h. Subsequently, different concentrations of Free Cel, Free BR, Cel-BR, and HA-RM-Cel-BR were added and incubated for an additional 24 h. The viability of RAW264.7 cells was assessed using a cell proliferation and cytotoxicity assay kit (Cell Counting Kit-8, CCK-8). Absorbance was measured at 450 nm using an enzyme marker, and the viability of the cells was calculated accordingly.

Cellular uptake and immune escape

The cellular uptake of nanomedicines was evaluated using coumarin-6 (Coumarin-6, Cou6, 150 ng/mL) as a fluorescent dye. RAW264.7 cells (3×10^5 cells/well) were inoculated into confocal Petri dishes (Biosharp, BS-20-GJM) and cultured for 12 h. After incubation, M1 macrophages were induced by stimulation with lipopolysaccharide (LPS) at a concentration of 500 ng/mL for an additional 12 h. Subsequently, different formulations

were co-incubated with the M1 macrophages for 2 h. The original medium was then removed, and the cells were washed with PBS. To fix the cells, 4% paraformaldehyde was applied for 10 min. The nuclei of the cells were stained using Hoechst 33,258 and imaged with a laser confocal microscope (CLSM, Leica, SP8). The fluorescence intensity of different formulations was quantified using flow cytometry (Beckman Coulter MoFlo Astrios EQ). The evaluation of immune escape was similar to that of cellular uptake, with the exception that RAW264.7 macrophages were not stimulated with LPS.

In *vivo* distribution of HA-RM-Cel-BR

Fluorescent dye 1,1'-bis(4-sulfobutyl)-3,3,3',3'-tetramethylindotricarbocyanine iodide (DIR) was administered at a dose of 1 mg/kg via tail vein injection to evaluate different formulations. In vivo imaging was performed at 6, 12, and 24 h post-injection using a small animal imaging system (Fusion-FX7 Spectra, France). Following the final imaging session, the rats were euthanized, and the major organs including the heart, liver, spleen, lungs, kidneys, and paws were excised for further imaging analysis.

Measurement of intracellular ROS and NO

RAW264.7 cells (8×10^3 cells/well) were inoculated into 96-well plates and cultured for 12 h, followed by stimulation with LPS (500 ng/mL) for an additional 12 h. The cells were then incubated in medium containing Free Cel (200 ng/mL), Free BR (3 μg/mL), Cel-BR (with a Cel concentration of 200 ng/mL), and HA-RM-Cel-BR (with a Cel concentration of 200 ng/mL) for 24 h. The cells without any treatment served as a negative control, while LPS-treated but untreated cells were used as a positive control. Subsequently, the cells were stained using a reactive oxygen species (ROS) detection kit, 2,7-dichlorofluorescein diacetate (DCFH-DA), and nitric oxide (NO) detection kit, 4-amino-5-methylamino-2,7-difluorofluorescein acetate (DAF-FM DA) for 30 min. Fluorescence images were captured using an inverted fluorescence microscope (Nikon Co., Japan).

Macrophage repolarization study

RAW264.7 cells (3×10^5 cells/well) were seeded in a 6-well plate and cultured for 12 h. M1 and M2 macrophages were induced using lipopolysaccharide (LPS) at 500 ng/mL concentrations and interleukin-4 (IL-4) at 20 ng/mL, respectively. After 12 h of stimulation, the cells were co-incubated with different formulations for 24 h. Subsequently, the cells were collected and incubated with anti-CD86-PE and anti-CD206-FITC antibodies for 30 min at 4 °C. After thorough washing, fluorescence intensity was measured using a flow cytometer (Beckman Coulter MoFlo Astrios EQ), and data analysis was conducted using FlowJo v10.8.1.

Anti-inflammatory activity in *vitro*

RAW264.7 cells (3×10^5 cells/well) were seeded in a 24-well plate and cultured for 12 h. Following this initial incubation, the cells were stimulated with 500 ng/mL LPS for an additional 12 h. Subsequently, different formulations (Free Cel, Free BR, Cel-BR, HA-RM-Cel-BR) were added, and the cells were treated for another 12 h. After treatment, the supernatant was collected, and the expression of inflammatory factors was measured using an ELISA kit.

Western blot analysis

Following protein extraction from RAW264.7 cells, separation was conducted using 4–20% sodium dodecyl sulfate-polyacrylamide gel electrophoresis (SDS-PAGE) at 150 V for 40 min. Subsequently, the samples were transferred to PVDF membranes for immobilization and incubated overnight at 4 °C with the corresponding primary antibodies: NF-κB, IκB-α, p-NF-κB, p-IκB-α, Nrf-2, Keap1, HO-1, STING and β-actin. The cells were then incubated with secondary antibodies for 2 h at room temperature and washed thrice. The signals were detected using Enhanced Chemiluminescence Liquid (ECL) and quantified using Image J.

Establishment of a rheumatoid arthritis model and Pharmacological evaluation

All animal experiments were approved by the Animal Protection and Use Committee of Ocean University of China (OUC-SMP-2024-02-15), and comply with the National Research Council's Guide for the Care and Use of Laboratory Animals. After 7 days of acclimatization, SD rats were subcutaneously injected with 80 μL of complete Freund's adjuvant in the right hind toe to establish an adjuvant-induced arthritis (AIA) model. The swelling was recorded daily, and treated with different formulations by tail vein injection on the 12th day. Rats were randomly divided into 6 groups: (1) Control; (2) Model (PBS treatment); (3) Free Cel (1 mg/kg); (4) Free BR (20 mg/kg); (5) Cel-BR (Cel at 1 mg/kg, BR at 20 mg/kg); (6) HA-RM-Cel-BR (Cel at 1 mg/kg, BR at 20 mg/kg). Treatments were administered by tail vein injection every 3 days.

Swelling was measured every 3 days using a toe volume measurement device, and the body weight of rats in different treatment groups was evaluated weekly. After the treatment, the right hind foot was functionally scored as described previously [35]. The hind paws of rats from different formulations were photographed, and a thermographic camera was utilized to capture the temperature of the paws. After euthanizing the rats, micro-computed tomography (Micro CT) was performed on the right hind foot (PerkinElmer, Quantum GX2, Japan) to evaluate the severity of bone erosion.

Statistical analysis

Data were analyzed and plotted using GraphPad Prism 9.5. Statistical analysis was performed using Student's t-test or one-way ANOVA in GraphPad Prism. Data are presented as mean ± standard deviation. Statistical significance was defined as $^{*}P < 0.05$, $^{**}P < 0.01$, and $^{***}P < 0.001$ compared to the specified group.

Abbreviations

RA	Rheumatoid arthritis
TCM	Traditional Chinese medicine
BR	Bilirubin
RM	Red blood cell membranes
Cel	Celastrol
ROS	Reactive oxygen species
RES	Reticuloendothelial system
HA	Hyaluronic acid
PBS	Phosphate Buffered Saline
MD	Molecular dynamics
RMSD	Root mean square deviation
SASA	Solvent-accessible surface area
^{1}H-NMR	Hydrogen nuclear magnetic resonance spectroscopy
DMSO-d6	Dimethyl sulfoxide-d6
D_2O	Deuterium oxide
Cou6	Coumarin 6
DIR	1,1′-Dioctadecyl-3,3,3′,3′-tetramethylindotricarbocyanine iodine
DCFH-DA	2′,7′-dichlorofluorescein diacetate
DAF-FM DA	4-amino-5-methylamino-2′,7′-difluorofluorescein diacetate
NO	Nitric oxide
WB	Western blotting
PCA	Principal component analysis
DEGs	Differentially expressed genes
KEGG	Kyoto Encyclopedia of Genes and Genomes
micro-CT	Micro-computed tomography
H&E	Hematoxylin and eosin
SO-FG	Senna O-Fixed Green
TRAP staining	Tartaric acid staining
PBS	Phosphate-buffered saline
ALP staining	Alkaline phosphatase staining
ALT	Aminotransferase
AST	Aspartate aminotransferase
CCK8	Cell Counting Kit-8
UV-vis	Ultraviolet-Visible Spectrophotometryp
FT-IR	Fourier Transform Infrared Spectroscopy
LPS	Lipopolysaccharide
SDS-PAGE	Sodium dodecyl sulfate-polyacrylamide gel electrophoresis

Supplementary Information

The online version contains supplementary material available at https://doi.org/10.1186/s12951-025-03389-9.

Supplementary Material 1

Supplementary Material 2

Supplementary Material 3

Supplementary Material 4

Supplementary Material 5

Supplementary Material 6

Supplementary Material 7

Graphical abstract

Acknowledgements

This work was supported by Shandong Provincial Natural Science Foundation (Grant ZR2024MH339).

Author contributions

Ynguo Su: Methodology, Conceptualization, Data curation, Writing-original draft, preparation. Rui Chen: Methodology, Investigation. Bingjie Wang: Software, Formal analysis. Teng Wang: Methodology, Formal analysis. Jiaojiao Tao: Conceptualization, Resources. Qijie Diao and Tianze Jiang: Methodology, Visualization. Xia Zhao: Project administration, Writing - review & editing, Funding acquisition, Supervision.

Data availability

No datasets were generated or analysed during the current study.

Declarations

Ethics approval and consent to participate

Protocols of animal experiments were permitted by Institutional Animal Care and Use Committee (IACUC), Ocean University of China.

Competing interests

The authors declare no competing interests.

Received: 26 February 2025 / Accepted: 14 April 2025
Published online: 26 April 2025

References

1. Smolen JS, Aletaha D, Barton A, Burmester GR, Emery P, Firestein GS, et al. Rheumatoid arthritis. Nat Rev Dis Primers. 2018;4:18001.
2. Lu Y, Zhou J, Wang Q, Cai J, Yu B, Dai Q, et al. Glucocorticoid-loaded pH/ROS dual-responsive nanoparticles alleviate joint destruction by downregulating the NF-κB signaling pathway. Acta Biomater. 2023;164:458–73.
3. Liu X, Chen S, Yan Y, Liu L, Chen Y. Nanoparticulate DNA scavenger loading methotrexate targets articular inflammation to enhance rheumatoid arthritis treatment. Biomaterials. 2022;286:121594.
4. Conigliaro P, Triggianese P, De Martino E, Fonti GL, Chimenti MS, Sunzini F, et al. Challenges in the treatment of rheumatoid arthritis. Autoimmun Rev. 2019;18:706–13.
5. Burmester GR, Pope JE. Novel treatment strategies in rheumatoid arthritis. Lancet. 2017;389:2338–48.
6. Lin Y, Tang Y, Yi O, Zhu J, Su Z, Li G, et al. Graphene oxide quantum dots-loaded Sinomenine hydrochloride nanocomplexes for effective treatment of rheumatoid arthritis via inducing macrophage repolarization and arresting abnormal proliferation of fibroblast-like synoviocytes. J Nanobiotechnol. 2024;22:383.
7. Jiang Z-M, Zeng S-L, Huang T-Q, Lin Y, Wang F-F, Gao X-J, et al. Sinomenine ameliorates rheumatoid arthritis by modulating Tryptophan metabolism and activating Aryl hydrocarbon receptor via gut microbiota regulation. Sci Bull (Beijing). 2023;68:1540–55.
8. Mao Q, Min J, Zeng R, Liu H, Li H, Zhang C, et al. Self-assembled traditional Chinese nanomedicine modulating tumor immunosuppressive microenvironment for colorectal cancer immunotherapy. Theranostics. 2022;12:6088–105.
9. Zhu Q, Zhou H. The role of cGAS-STING signaling in rheumatoid arthritis: from pathogenesis to therapeutic targets. Front Immunol. 2024;15:1466023.
10. Lu B, Li C, Jing L, Zhuang F, Xiang H, Chen Y, Huang B. Rosmarinic acid nanomedicine for rheumatoid arthritis therapy: targeted RONS scavenging and macrophage repolarization. J Control Release. 2023;362:631–46.
11. Ma Y, Lu Z, Jia B, Shi Y, Dong J, Jiang S, Li ZDNA. Origami as a nanomedicine for targeted rheumatoid arthritis therapy through reactive oxygen species and nitric oxide scavenging. ACS Nano. 2022;16:12520–31.
12. Geng W, Liu X, Tao B, He Y, Li K, Gao P et al. Nitric oxide scavenging and hydrogen sulfide production synergistically treat rheumatoid arthritis. Adv Healthc Mater. 2023;12:e2202380.
13. Shen H, Jin L, Zheng Q, Ye Z, Cheng L, Wu Y, et al. Synergistically targeting synovium STING pathway for rheumatoid arthritis treatment. Bioact Mater. 2023;24:37–53.

14. Sun S, Lv W, Li S, Zhang Q, He W, Min Z, et al. Smart liposomal nanocarrier enhanced the treatment of ischemic stroke through neutrophil extracellular traps and Cyclic Guanosine monophosphate-Adenosine monophosphate Synthase-Stimulator of interferon genes (cGAS-STING) pathway Inhibition of ischemic penumbra. ACS Nano. 2023;17:17845–57.
15. Yuan R, Li Y, Han S, Chen X, Chen J, He J et al. Fe-Curcumin Nanozyme-Mediated reactive oxygen species scavenging and Anti-Inflammation for acute lung injury. ACS Cent Sci. 2022;8:10–21.
16. Fan M, Zheng X, Cheng W, Wei H, Li P, Ji C, Yin M. Reinforcing Carrier-Free photothermal nanodrugs through Flavonol-Driven assembly. Adv Funct Mater. 2024:2402455.
17. Fan D, Guo Q, Shen J, Zheng K, Lu C, Zhang G, et al. The effect of triptolide in rheumatoid arthritis: from basic research towards clinical translation. Int J Mol Sci. 2018;19:376.
18. Liu Y, Xiao N, Du H, Kou M, Lin L, Huang M, et al. Celastrol ameliorates autoimmune disorders in Trex1-deficient mice. Biochem Pharmacol. 2020;178:114090.
19. Yang N, Li M, Wu L, Song Y, Yu S, Wan Y, et al. Peptide-anchored neutrophil membrane-coated biomimetic nanodrug for targeted treatment of rheumatoid arthritis. J Nanobiotechnol. 2023;21:13.
20. Lu S, Li Y, Yu Y. Glutathione-Scavenging Celastrol-Cu nanoparticles induce self-amplified cuproptosis for augmented cancer immunotherapy. Adv Mater. 2024:e2404971.
21. Li Z, Liu R, Zhang X, Guo Z, Geng X, Chu D, et al. An injectable thermoresponsive-hydrogel for lamellar keratoplasty: In-situ releases Celastrol and hampers corneal scars. J Control Release. 2024;369:604–16.
22. Du X, Li C, Zhang S, Sun C, Zhang X, Chen C, et al. Exploring the Pharmacological mechanism of calculus Bovis in cerebral ischaemic stroke using a network Pharmacology approach. J Ethnopharmacol. 2022;284:114507.
23. Yu Z-J, Xu Y, Peng W, Liu Y-J, Zhang J-M, Li J-S, et al. Calculus Bovis: A review of the traditional usages, origin, chemistry, Pharmacological activities and toxicology. J Ethnopharmacol. 2020;254:112649.
24. Hua P, Liang R, Tu Y, Yin Y, Law M-K, Chen M. Reactive oxygen species and nitric oxide scavenging nanoparticles alleviating rheumatoid arthritis through adjusting the seeds and growing soils. Acta Pharm Sin B. 2023;13:5016–29.
25. Yao Q, Tang Y, Dai S, Huang L, Jiang Z, Zheng S, et al. A biomimetic nanoparticle exerting protection against acute liver failure by suppressing CYP2E1 activity and scavenging excessive ROS. Adv Healthc Mater. 2023;12:e2300571.
26. Fu S, Yi X, Li Y, Li Y, Qu X, Miao P, Xu Y. Berberine and chlorogenic acid-assembled nanoparticles for highly efficient Inhibition of multidrug-resistant Staphylococcus aureus. J Hazard Mater. 2024;473:134680.
27. Chang Z, Chen D, Peng J, Liu R, Li B, Kang J, et al. Bone-Targeted supramolecular nanoagonist assembled by accurate ratiometric Herbal-Derived therapeutics for osteoporosis reversal. Nano Lett. 2024;24:5154–64.
28. Xiong H, Zhang H, Qin Y, Ye J, Zeng F, Xie P, et al. Coassembly nanomedicine mediated by intermolecular interactions between methotrexate and baricitinib for improved rheumatoid arthritis treatment. ACS Nano. 2024;18:8337–49.
29. Wan Y, Li C, Fu L-H, Feng T, Zhang Y, Li Y et al. Erythrocyte membrane camouflaged nanotheranostics for optical molecular imaging-escorted self-oxygenation photodynamic therapy. Small. 2024:e2309026.
30. Chen J, Liu S, Li Y, Zhang S, Li X, Wang J. Erythrocyte membrane-camouflaged and double-factor sequential delivery nanocarriers postpone the progression of osteoarthritis. Chem Eng J. 2023;473:145180.
31. Gu J, Yan C, Yin S, Wu H, Liu C, Xue A, et al., et al. Erythrocyte membrane-coated nanocarriers modified by TGN for Alzheimer's disease. J Controlled Release. 2024;366:448–59.
32. Wang P, Zhang Y, Lei H, Yu J, Zhou Q, Shi X, et al. Hyaluronic acid-based M1 macrophage targeting and environmental responsive drug releasing nanoparticle for enhanced treatment of rheumatoid arthritis. Carbohydr Polym. 2023;316:121018.
33. Yang Y, Liu Q, Wang M, Li L, Yu Y, Pan M, et al. Genetically programmable cell membrane-camouflaged nanoparticles for targeted combination therapy of colorectal cancer. Signal Transduct Target Ther. 2024;9:158.
34. Gao C, Huang Q, Liu C, Kwong CHT, Yue L, Wan J-B et al. Treatment of atherosclerosis by macrophage-biomimetic nanoparticles via targeted pharmacotherapy and sequestration of Proinflammatory cytokines. Nat Commun. 2020;11:2622.
35. Zhou F, Li M, Chen M, Chen M, Chen X, Luo Z, et al. Redox homeostasis strategy for inflammatory macrophage reprogramming in rheumatoid arthritis based on ceria oxide Nanozyme-Complexed biopolymeric micelles. ACS Nano. 2023;17:4358–72.
36. Sun J, Zhao X, Shen H, Dong J, Rong S, Cai W, Zhang R. CD44-targeted melanin-based nanoplatform for alleviation of ischemia/reperfusion-induced acute kidney injury. J Controlled Release. 2024;368:1–14.
37. Chadha S, Behl T, Kumar A, Khullar G, Arora S. Role of Nrf2 in rheumatoid arthritis. Curr Res Transl Med. 2020;68:171–81.
38. Xue G, Jiang H, Song Z, Zhao Y, Gao W, Lv B, Cao JD. Targeting biomimetic Carrier-Free nanosystems for Photo-Chemotherapy of rheumatoid arthritis via macrophage apoptosis and Re-Polarization. Adv Sci (Weinh). 2025:e2406877.
39. Rossini M, Adami G, Viapiana O, Idolazzi L, Gatti D. Denosumab, cortical bone and bone erosions in rheumatoid arthritis. Ann Rheum Dis. 2016;75:e70.
40. Siddiqui B, Ur Rehman A, Gul R, Chaudhery I, Shah KU. Ahmed N.Folate decorated chitosan-chondroitin sulfate nanoparticles loaded hydrogel for targeting macrophages against rheumatoid arthritis. Carbohydr Polym. 2024;327:121683.
41. Wu X, Guo H, Gao H, Li Y, Hu X, Kowalke MA, et al. Peptide targeting improves the delivery and therapeutic index of glucocorticoids to treat rheumatoid arthritis. J Control Release. 2024;368:329–43.
42. Zheng L, Chen Y, Gu X, Li Y, Zhao H, Shao W, et al. Co-delivery of drugs by adhesive transdermal patches equipped with dissolving microneedles for the treatment of rheumatoid arthritis. J Control Release. 2024;365:274–85.
43. An X, Yang J, Cui X, Zhao J, Jiang C, Tang M, et al. Advances in local drug delivery technologies for improved rheumatoid arthritis therapy. Adv Drug Deliv Rev. 2024;209:115325.
44. Chen S-X, Xue F, Kuang Y, Chen S, Sheng D, Chen H. A self-activating nanovesicle with oxygen-depleting capability for efficient hypoxia-responsive chemo-thermo cancer therapy. Biomaterials. 2021;269:120533.
45. Khan TZ, Newaj SM, Rahman A, Tabassum R, Tasnim KN, Reza HM et al. NIR-light-triggered delivery of doxorubicin-loaded PLGA nanoparticles for synergistic cancer therapy on DMBA/TPA induced tumor-bearing mice. Mater Adv. 2023;4:5175–83.
46. Sharker SM, Kim SM, Kim SH, In I, Lee H, Park SY. Target delivery of β-cyclodextrin/paclitaxel complexed fluorescent carbon nanoparticles: externally NIR light and internally pH sensitive-mediated release of Paclitaxel with bio-imaging. J Mater Chem B. 2015;3:5833–41.
47. Lin Y, Yi O, Hu M, Hu S, Su Z, Liao J, et al. Multifunctional nanoparticles of Sinomenine hydrochloride for treat-to-target therapy of rheumatoid arthritis via modulation of Proinflammatory cytokines. J Control Release. 2022;348:42–56.
48. Cui J, Wang X, Li J, Zhu A, Du Y, Zeng W, et al. Immune exosomes loading self-assembled nanomicelles traverse the blood–brain barrier for chemo-immunotherapy against glioblastoma. ACS Nano. 2023;17:1464–84.

Publisher's note